Experimental and numerical modelling studies for rockburst assessment

Carlos Enrique Rojas Perez

Department of Mining and Materials Engineering

McGill University, Montreal

March 2025

A thesis submitted to McGill University in partial fulfillment of the requirements of a degree of Master of Engineering in the Department of Mining and Materials Engineering.

Abstract

Rockburst control in underground mines is a challenging problem, especially in deep metal mines with high ore extraction ratio. The increased likelihood of rockburst occurrence can be a cause for safety concerns to the mine operators. The parameters associated with rockbursts are generally related to geological features such as dykes and faults, mechanical rock properties, seismic activities, and production rates. Mining aspects such as stope sequence, mining direction, stope geometry, backfill material, and the mining method all contribute to the occurrence of rockburst. This thesis investigates rockburst potential at two underground mines in northern Ontario, namely Macassa Mine of Agnico Eagle Mines Ltd and Young Davidson (YD) Mine of Alamos Gold Inc. The thesis begins with a comprehensive literature review of rockburst assessment methods.

The first case study of Macassa Mine is of a sill pillar situated 5,600 feet (1,700 m) below surface. It is 360 feet (110 m) long and 50 feet (15.5 m) in height, with a varying thickness averaging 3 m. The sill pillar is planned for extraction with longhole stoping in retreat. Past mining activities employed cut-and-fill methods. The levels above and below the sill pillar are tight filled with pastefill. To assess the stress condition in the pillar, a 3D mine wide numerical model was created with FLAC3D finite difference code. The numerical model employs the Macassa geomechanical database and in-situ stress regime. Pillar burst conditions are assessed using the deviatoric stress ratio, also known as the brittle shear ratio (BSR), to estimate potential brittle shear failure, and the burst potential index (BPI) based on energy considerations to examine strainburst potential. Model calibration relied on microseismic monitoring activities in the sill pillar over the past year. Rockburst mitigation and control methods with dynamic support in the sill drives are discussed.

The second case study of the YD Mine focused on the lower mine in the depth range of 900 m to 1200 m below surface where strong seismic events were recorded. The study first required laboratory testing for the determination of mechanical rock properties and rock burstability. Rock core samples were acquired from different lithologies namely syenite, porphyry syenite, basalt, diabase, sheared sediments and sediments. The experimental program involved uniaxial compressive strength (UCS), Brazilian tensile strength (BTS) tests, and uniaxial load-unload (LUN) tests to help determine rock burstability by loading the rock sample to 70-85% of its UCS then unloading it. A FLAC3D numerical model was then updated with the new geomechanical

properties and used for stress analysis. The numerical model simulates mining-induced stress distribution while following the history of stope extraction. Assessment is conducted using the BSR. The study revealed that strong seismic activities are attributed mainly to high pre-mining differential stress ($\sigma_1^0 - \sigma_3^0$) with σ_1^0 running in the NE direction at an oblique angle to the orebody.

Résumé

Le contrôle des coups de terrain dans les mines souterraines est un problème difficile, en particulier dans les mines de métaux profondes où le taux d'extraction du minerai est élevé. L'augmentation de la probabilité des coups de terrain de roches peut être une source d'inquiétude pour la sécurité des exploitants miniers. Les paramètres associés aux coups de terrain sont généralement liés aux caractéristiques géologiques telles que les dykes et les failles, aux propriétés mécaniques des roches, aux activités sismiques et aux taux de production. Les aspects de l'exploitation minière tels que la séquence des chantiers, la direction de l'exploitation, la géométrie des chantiers, les matériaux de remblayage et la méthode d'exploitation minière contribuent tous à la survenue de ces événements. Cette thèse étudie le potentiel de coups de terrain dans deux mines souterraines du nord de l'Ontario, à savoir la mine Macassa d'Agnico Eagle Mines Ltd et la mine Young Davidson (YD) d'Alamos Gold Inc. La thèse commence par une revue documentaire complète des méthodes d'évaluation des coups de terrain.

La première étude de cas de la mine de Macassa porte sur un pilier situé à 5 600 pieds (1,700 m) sous la surface. Il mesure 360 pieds (110 m) de long et 50 pieds (15,5 m) de haut, avec une épaisseur variable de 3 m en moyenne. L'extraction est planifiée par abattage par long trou en retrait. Les activités minières passées ont utilisé des méthodes de déblai et remblai. Les niveaux au-dessus et au-dessous du pilier sont remplis de pâte. Pour évaluer les conditions de contrainte dans le pilier, un modèle numérique 3D à l'échelle de la mine a été créé avec le code de différences finies FLAC3D. Le modèle numérique utilise la base de données géomécaniques de Macassa et le régime de contraintes in situ. Les conditions d'éclatement du pilier sont évaluées à l'aide du rapport de contrainte déviatorique, également connu sous le nom de rapport de cisaillement fragile (BSR), pour estimer la rupture potentielle par cisaillement fragile, et l'indice de potentiel d'éclatement (BPI) basé sur des considérations énergétiques pour examiner le potentiel d'éclatement par déformation. L'étalonnage du modèle s'est appuyé sur les activités de surveillance microsismique du pilier au cours de l'année écoulée. Les méthodes d'atténuation et de contrôle des coups de terrain avec un support dynamique dans les piliers sont discutées.

La deuxième étude de cas de la mine YD s'est concentrée sur la partie inférieure de la mine, à une profondeur comprise entre 900 et 1200 m sous la surface, où de fortes secousses sismiques ont été

enregistrées. L'étude a d'abord nécessité des essais en laboratoire pour déterminer les propriétés mécaniques de la roche et sa capacité des coups de terrain. Des carottes de roche ont été prélevées ont été prélevés dans différentes lithologies: syénite, syénite porphyrique, basalte, diabase, sédiments cisaillés et sédiments. Le programme expérimental comprenait des essais de résistance à la compression uniaxiale (UCS), de résistance à la traction brésilienne (BTS) et des essais de charge et décharge uniaxiale (LUN) pour aider à déterminer l'éclatement de la roche en chargeant l'échantillon de roche à 70-85% de son UCS puis en le déchargeant. Un modèle numérique FLAC3D a ensuite été mis à jour avec les nouvelles données géomécaniques et utilisé pour l'analyse des contraintes. Le modèle numérique simule la distribution des contraintes induites par l'exploitation minière tout en suivant l'historique de l'extraction des chantiers. L'évaluation est réalisée à l'aide du BSR. L'étude a révélé que les fortes activités sismiques sont principalement attribuées à des contraintes différentielles élevées avant l'exploitation ($\sigma_1^0 - \sigma_3^0$)), σ_1^0 s'étendant dans la direction NE à un angle oblique par rapport au corps minéralisé

Acknowledgments

To begin with, I want to thank my thesis supervisor, Prof. Hani Mitri, to whom I feel extremely grateful. He believed in me and enabled me to get this invaluable opportunity to do my masters. His support was continuous throughout the path and his great guidance made me challenge myself to keep on working and follow my passion about mining. During this journey, he was a key component of making this possible as his knowledge, experience and advice made this thesis possible.

This thesis was financially supported by the Natural Science and Engineering Research Council of Canada (NSERC) – Discovery Program. It was also supported by Alamos Gold Inc. through a MITAC Accelerate Project No. IT30669 ACC. I am grateful for their financial support. Also, I would like to thank Travis Blake and Hugo Ferrari from the Young Davidson Mine for their technical support and encouragement. I am grateful for the training opportunity at YD Mine and I firmly believe it will help me throughout my career.

I would also like to thank my colleagues from the Mine Design Laboratory, Yizhuo Li, Tuo Chen, Kenneth Adams, Patrick Darko and Elvis Mensah for the time we spent together. The time we had as a group was important for me for all the advice, experiences, and thoughts we were able to share.

To my friends Christian, Joseph, Francisco, Juan, Fabrizio, and Kevin for their support through this thesis. The time we spent together, and the experiences are something I cherish a lot, and I will always remember this process as an overall learning experience. And for my role models Renzo, Gabriel and my uncle Belisario who I always aim to become one day. Without their advice, I wouldn't have taken this opportunity.

Finally, I would love to express my eternal gratitude to my dear family for their understanding and encouragement through this process. To my older brother and sister, my cousin Diego, my beloved younger brothers Jorge and Benjamin for the smiles we shared together. And a special thanks to my mom Marlene and dad Hernan who always supported me in every aspect of my life and to whom I may never be able to pay back all the deeds they have done for me in this life. But I still have a life ahead to give to them.

Contribution of Authors

Chapters 1, 2 and 4 are contributions of the author in their entirety. Chapter 3 is a jointly published journal paper of which the thesis author is the first author.

- Rojas Perez, C., Wei, W., Gilvesy, A., Borysenko, F., Mitri, H. 2024. Rockburst assessment and control: a case study of a deep sill pillar recovery. Deep Mining 2024.

The specific contributions of each co-author to the abovementioned paper are as follows.

- Rojas Perez: Conceptualization, methodologies, analysis, production of the first draft, visualization, processing of the data.
- Wei, Gilvesy and Borysenko: Review for confidential information, processing and accuracy of the field observations, recommendations.
- Mitri: Supervision, funding, final review.

Chapter 5 is submitted to the Journal of Deep Resources Engineering.

- Rojas Perez, C., Ferrari, H., Mitri, H. 2025. Effect of mining geometry on mining induced burst events – A case study. Rock Mechanics and Rock Engineering.

The specific contributions of each co-author to the abovementioned paper are as follows.

- Rojas Perez: Conceptualization, methodologies, analysis, production of the first draft, visualization, processing of the data.
- Ferrari: Review for confidential information, processing and accuracy of the field observations, recommendations.
- Mitri: Supervision, funding, final review.

Table of contents

List of Figures

List of Tables

Chapter 1 - Introduction

1.1 Background

Rockbursts are becoming increasingly frequent as mining companies around the world continue to reach deeper deposits and mine at higher ore extraction ratio leaving little or no pillar supports within the orebody. Rockbursts are usually more frequent in deep mines, but they can also take place in shallow mines (Li et al., 2019). These events can pose safety threats as they can result in personnel injuries or even fatalities. Rockbursts can have a negative impact on the economics of a mining operation due to production delays, equipment damage, and loss of the workforce productivity due to anxiety over on-shift rockburst occurrence. As a result, there has been a lot of research in recent years on rockburst phenomena and their prediction as well as the damage they can cause (Zhou et al., 2018). In Canada, the occurrence of rockbursts is equally frequent and is on the rise since they were first recorded in the 1930s in Sudbury and Kirkland Lake (Hasegawa et al., 1989).

There are many reports of rockburst events throughout the world. South Africa has been suffering from rockburst phenomena in their deep mines since the early 20th Century. These events were mostly related to mining-induced seismicity. The largest seismic event reported is at the Klerksdorp District in South Africa in 2005 with a magnitude of 5.3 on the Ritcher Scale causing injuries to operators and buildings (Durrheim, 2010). In China, especially in coal mines, there has been an overall increase in the number of rockburst events with the major issue being the high stress accumulation due to longwall mining. The first event documented in China was reported in 1933 at the Fushun Mining area. A total of 212 rockburst events were reported across the mines in China in 2018 representing a significant increase over the previous years. Between 2012 and 2022, and despite incomplete statistics then, 13 rockburst incidents were reported in China with consequences of nearly 100 deaths and 1000 injuries (Rong et al., 2022). There are many other documented rockburst cases in countries such as Australia (Heal and Potvin, 2006), Russia (Adushkin et al., 2022), and Chile (Ortlepp, 2005). Thus, the study of rockbursts will remain relevant in future since the global trend is towards deep and pillarless mining. This makes it important to develop the right tools and techniques to predict rock burstability and rockburst occurrence to act accordingly without major setback to the operation. Figure 1.1 shows the

geographical distribution of countries suffering from rockburst phenomena around the world (Wu et al., 2022).

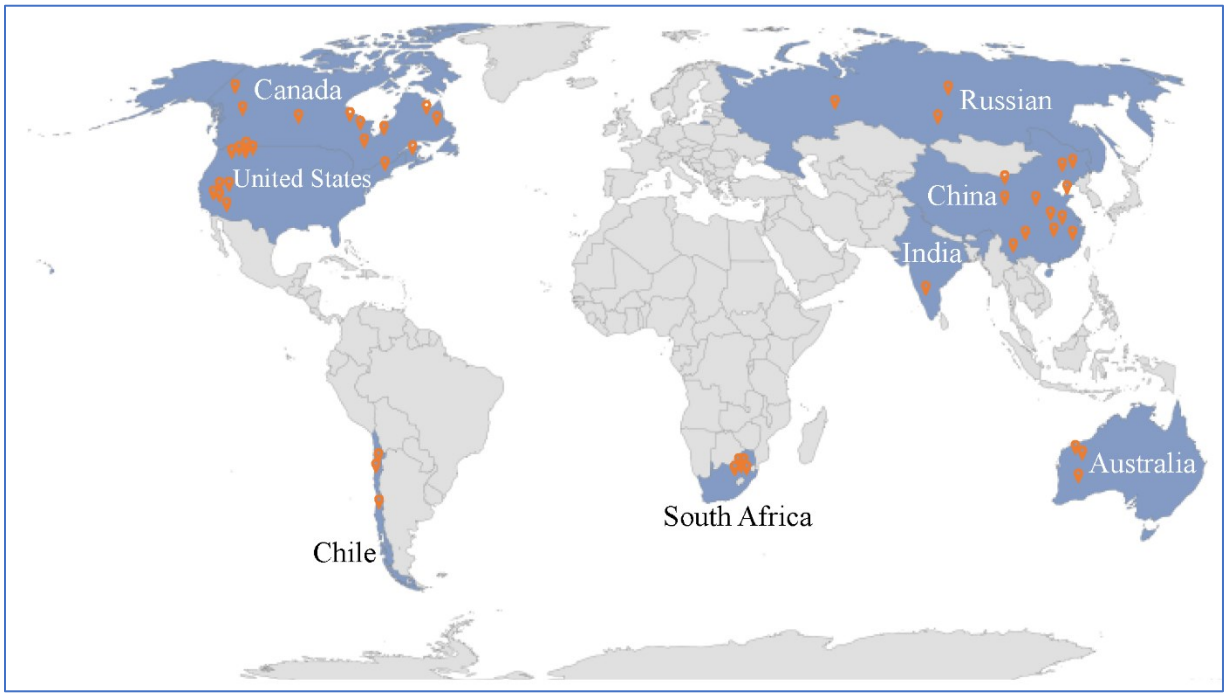

Figure 1.1: Geographical distribution of countries suffering from rockburst phenomena (Wu et al., 2022).

Rockbursts have been studied by various authors throughout the years; several classifications were proposed over the decades to further detail into the different scenarios where they were found. However, most authors agree that there are 3 major categories: at-face bursts, large-mass bursts and far-field bursts (Mitri, 2018).

At-face bursts are, in most cases, related to sudden release of energy and high stress at the mining face. These events may cause local damage since they tend to not be of large seismic moment magnitude. It is also common to relate this kind of burst to strainbursts. Cook (1965) defined rockburst as violent release of energy in underground mines and defined strainburst as one of the possible events. Ortlepp (1997) proposed the term ‘strainburst’ for one of the types of rockburst events which take place in the faces of the excavations. Mitri et al. (1999), and Castro et al. (2012) also related the strainbursts to these events in their research.

Large-mass events are more related to higher volumes of rock mass and often refer to ore pillars in metal mines. The amount of energy is higher, and it is common to have the sudden release of

more seismic energy. Lastly, far-field events are related to violent shear rupture of geological structures like dykes or shear slip along faults or other similar geological structures. Hedley (1992), Ortlepp (1997) and Mitri et al. (1999) defined these events as fault-slips and added that these burst events usually occur because of slippage along pre-existing faults. These events tend to not occur near the mining face. Nevertheless, due to the amount of energy released, the seismic waves can reach the free mining face and cause damage to the mine openings.

Many attempts to consistently predict and classify the rockburst potential in underground mines have been made (Zhou et al., 2018). Among the many approaches, the most relevant ones are associated with energy and strength. These approaches are related mostly to empirical models which could be later validated by numerical models. The success of these methodologies is closely tied to how well they represent the combination of the properties of the rock, in-situ stresses, geological structures, and the geometric properties of the mining method. However, there are certain cases where the rock mass properties are not strictly prone to bursting, however, a series of strain bursts is observed in the field. These cases are often related to the mine geometry, more specifically the last production stope in a planned sequence resulting in a highly stressed ore pillar. This type of rockburst event is primarily dictated by the geometry of the stopes/pillars.

The first case study in this thesis is of a sill pillar at Macassa Mine of Agnico Eagle Mines Ltd. The pillar is situated 5,600 feet (1,700 m) below the ground surface. It is 360 feet (110 m) long and 50 feet (15.5 m) in height, with a varying thickness averaging 3 m. Past mining activities employed cut-and-fill methods. The levels above and below the sill pillar are tight-filled with pastefill. To assess the stress condition in the pillar, a 3D mine wide numerical model was created with FLAC3D finite difference code. The numerical model employs the Macassa geomechanical database and in-situ stress regime. Model calibration relied on microseismic monitoring activities in the sill pillar over the past year. Rockburst mitigation and control methods with dynamic support in the sill drives are discussed.

The second case study of this thesis is from the Young Davidson (YD) Mine of Alamos Gold Inc. The study needed laboratory testing to be carried out for the determination of mechanical rock properties of different lithologies. Rock core samples were acquired from different lithologies namely syenite, porphyry syenite, basalt, diabase, sheared sediments and sediments. The experimental program involved primarily uniaxial compressive strength (UCS)

and Brazilian tensile strength (BTS) tests. Moreover, uniaxial load-unload (LUN) tests were conducted to help determine rock burstability by loading the rock sample to 70-85% of its UCS then unloading it. A previously built mine wide FLAC3D numerical model was then updated with the new geomechanical properties and used for stress analysis. The YD mine is experiencing large seismic events at different mining horizons. The focus is the lower mine in the depth range of 900 m to 1200 m below surface where strong seismic events were recorded. In-situ stress measurements previously conducted at the YD mine were used. The numerical model simulates mining-induced stress distribution while following the mine plan of primary and secondary stope extraction. Assessment is conducted using the BSR. Figure 1.2 shows the locations of both mines in Northern Ontario.

Figure 1.2: Location map of the case study mines - Young-Davidson Mine and Macassa Mine in Northern Ontario (produced using Google Map).

1.2 Scope and objectives

Many Canadian mining companies operate at depths reaching or exceeding 1 km. Due to the nature of the high tectonic stresses found in the Canadian PreCambrian Shield as well as the presence of strong and brittle hard rock formations, underground metal mines frequently encounter rockburst events. In this study, numerical modelling and rock property testing are used to help assess rock burst potential at two Canadian underground mines namely Macassa Mine and YD Mine. The main objectives of this thesis can be summarized as follows.

1. A comprehensive literature review on rock burstability criteria covering the parameters associated with rockbursts such as geological features, mechanical rock properties and mining parameters.
2. Evaluation of burst potential due to the recovery of a deep sill pillar at Macassa Mine. Rockburst potential is evaluated by developing a large-scale mine wide numerical modelling with FLAC3D code and using the Burst Potential Index (BPI) (Mitri et al., 1999) and the Brittle Shear Ratio (BSR) (Castro et al., 2012).
3. Design and carry out a comprehensive experimental program to determine the mechanical rock properties from different lithologies at YD Mine. Additionally, load-unload (LUN) tests are conducted for the determination of rock burstability index (Kidybinski, 1981). The results are used to update the geomechanical database of YD Mine.
4. Elaboration of a previously developed FLAC3D model of Young-Davidson Mine using the updated geomechanical database taking into consideration the past and planned mining sequence. Stress analysis results are used to help interpret the root causes for the recorded seismic events using the BSR criterion (Castro et al., 2012) and the results of moment tensor inversion analysis (Khalil, 2023).

1.3 Thesis Structure

This thesis consists of seven chapters which are organized as follows. Chapter 1 is an introduction; it presents the background and scope and objectives of this thesis. Chapter 2 is a comprehensive literature review on both empirical and theoretical rock burstability criteria which are well established in the literature. Chapter 3 is a published paper of a case study on the recovery of a deep sill pillar assessing rockburst potential and control at Macassa Mine. It describes the analysis of the stability of a deep sill pillar at Macassa mine considering the rockburst criteria presented in Chapter 2. Chapter 4 describes the experimental program for the characterization of the lithologies from Young-Davidson Mine. Rock cores were tested to determine their mechanical properties. Chapter 5 is a paper submitted to the Journal of Deep Resources Engineering. It presents the 3D stress analysis of the YD Mine using the updated geomechanical database and delineates the principal causes for mining-induced seismicity. Chapter 6 summarizes the conclusions drawn from the two case studies and highlights suggestions for future work.

Chapter 2 - Literature Review

2.1 Introduction

There are multiple definitions of rockburst in the literature. However, most definitions agree that rockburst events are sudden and violent occurrences of rock failure (Ortlepp, 1997). Some authors relate the definition of rockburst to the sudden release of energy and microseismic activity as it is always related to both (Cook, 1965). Most keywords from different authors relate rockburst events to high stress, brittle rock, seismic events, and strong rocks.

Although rockbursts are always related to seismic activities, not all seismic activities lead to rockburst events (Martin & Chandler, 1996). Ortlepp (1992) proposed a classification based on the types of rockburst commonly found in South African mines. His classification related the Richter magnitude of the seismic event to the type of rockburst expected. As shown in Table 2.1, strain bursting is related to lower magnitudes while fault-slip is related to higher magnitudes on the Richter scale. It is important to note that strainbursts and bucking, while associated with small magnitude events < 1.5, they can still cause damage in the form of violent ejections into the mine opening. On the other hands, large events > 2 are often the result of a shear mechanism, known as double-couple in geological faults and shear zones.

Table 2.1: Classification of rockburst types proposed by Ortlepp (1992).

Seismic event	Postulated source mechanism	First motion seismic records	Richter magnitude M_L
Strain Bursting	Superficial spalling with violent ejections of fragments	Usually undetected, could be implosive	-0.2 to 0
Buckling	Outward expulsion of larger slabs pre-existing parallel to opening	Implosive	0 to +1.5
Pillar or face crush	Violent expulsion of rock from tunnel face or pillar	Implosive	+1.0 to +2.5

Shear rupture	Violent propagation of shear fracture through intact rock mass	Double-couple shear	+2.0 to +3.5
Fault-slip	Violent renewed movement on existing fault	Double-couple shear	+2.5 to +5.0

Ortlepp (1994) further described strainbursts as common occurrence creating fragments of rock, usually in form of thin plates that are violently ejected from the rock surface (Ortlepp, 1994). Pillar or face crushes are more violent and the ejection from the rocks tend to be larger in comparison to strainbursts. Buckling is related to failure of laminated rock fabric which can undergo buckling when found parallel to the excavation sidewalls.

The classification given by Ortlepp (1992) is relevant because it relates directly the energy involved in seismic events to a specific source mechanism. This enables a better understanding of the stress, geological conditions and more importantly, the mining influence on the rock failure process. Keneti and Sainsbury (2018) reviewed historical cases of rockburst, and identified possible drivers which may contribute to the occurrence of rockburst events.

A relevant observation was made regarding strain bursting by Ortlepp (1994) and that is strain bursting is not an event exclusively related to brittle rocks. This observation suggests that the material properties can sometimes be less prone to burst, however, can still play an important role in the occurrences of rockburst events.

One of the studies most referred to nowadays is the work by Kaiser and Cai (2018) divides rockburst causes into 4 main categories: geotechnical, geologic, mining, and seismic. Geotechnical parameters in this classification are related to in-situ stress where their magnitude and the ratios between the major and minor principal stress play an important role. They are also related to the mechanical properties of the rock like strength, brittleness, and rockmass rating. Geologic parameters refer to geological features such as dykes and shear zones. Such structures often produce high local stresses causing stress concentration and rock failure. Alteration of rock is also commonly found near geological structures, e.g. fault damage zone. There are also cases of anisotropy due to the presence of foliation and beddings which could influence the failure mechanism.

Mining parameters, as a cause for rockburst, are mostly related to the disruption of the in-situ stresses values due to mining activities. Mining causes stress relaxation and stress concentration in different zones around the production area. The sequence of stope production leading to rockburst events has become more common. Backfill is another important aspect to take into consideration since it may greatly improve confinement and stress redistribution.

Finally, seismic activity as a primary cause for rockburst Kaiser and Cai (2018) is dependent on event magnitude, distance to seismic source, and the rate of seismic energy release.

The prediction of rockburst occurrence is paramount for the safety of the operation and the personnel. Over the years, there has been a lot of research on how to predict the likelihood of these events to occur. This is discussed in more detail in the next section.

2.2 Rockburst prediction criteria based on mechanical rock properties

One way to characterize the potential of rockburst events is by using the mechanical properties of the rock to determine its proneness to burst. Parameters such as brittleness and strain energy are relevant to determining the likelihood of a bursting behaviour. As the occurrence of rockburst depends greatly on the capacity of the rock to store strain energy (Wang and Park, 2001), estimating the energy accumulated due to mining activities can be helpful. The ratio of these two energy quantities is defined as the burst potential index or BPI (Mitri et al., 1999). Amongst the energy-based criteria, there are 2 main approaches: Strain Energy Storage Index (W_{et}) proposed by Kidybinski (1981), and Strain Energy Density (SED) proposed by (Wang and Park, 2001). The rock brittleness, assessed with the Brittleness index (B) (refences), is also relevant. These are further explained below.

2.2.1 Strain Energy Storage Index

The Strain Energy Storage (W_{et}) index was first proposed as a relation between the recovered elastic energy and the plastic energy in a load-unload, uniaxial compressive test (Neyman et al. 1972).

$$W_{et} = \frac{W_r}{W_p} \tag{2.1}$$

In equation 2.1, W_r is the recovered energy defined by the area under the unloading curve on the unloading phase while performing a load-unload test, and W_p is the plastic energy defined by the area surrounded between the loading and unloading curves as shown in Figure 2.1 from Malki et al. (2024).

To obtain the energy quantities in equation 2.1, a non-destructive load-unload test is necessary, whereby the uniaxial loading can be in the range of 80-90% of the peak compressive strength. The assumption is that the mechanical energy responsible for rockburst is related to the elastic strain energy stored in a highly-stressed rock.

Two authors proposed ranges to consider burstability based on the W_{et} index, Kidybinski (1981) proposed values for the case of coal mines with rockbursting problems as shown in Table 2.2. His observations showed that coal with a W_{et} index > 5 failed violently with a wide spread of chips, while values between 2 and 5 only showed ductile failure behaviour.

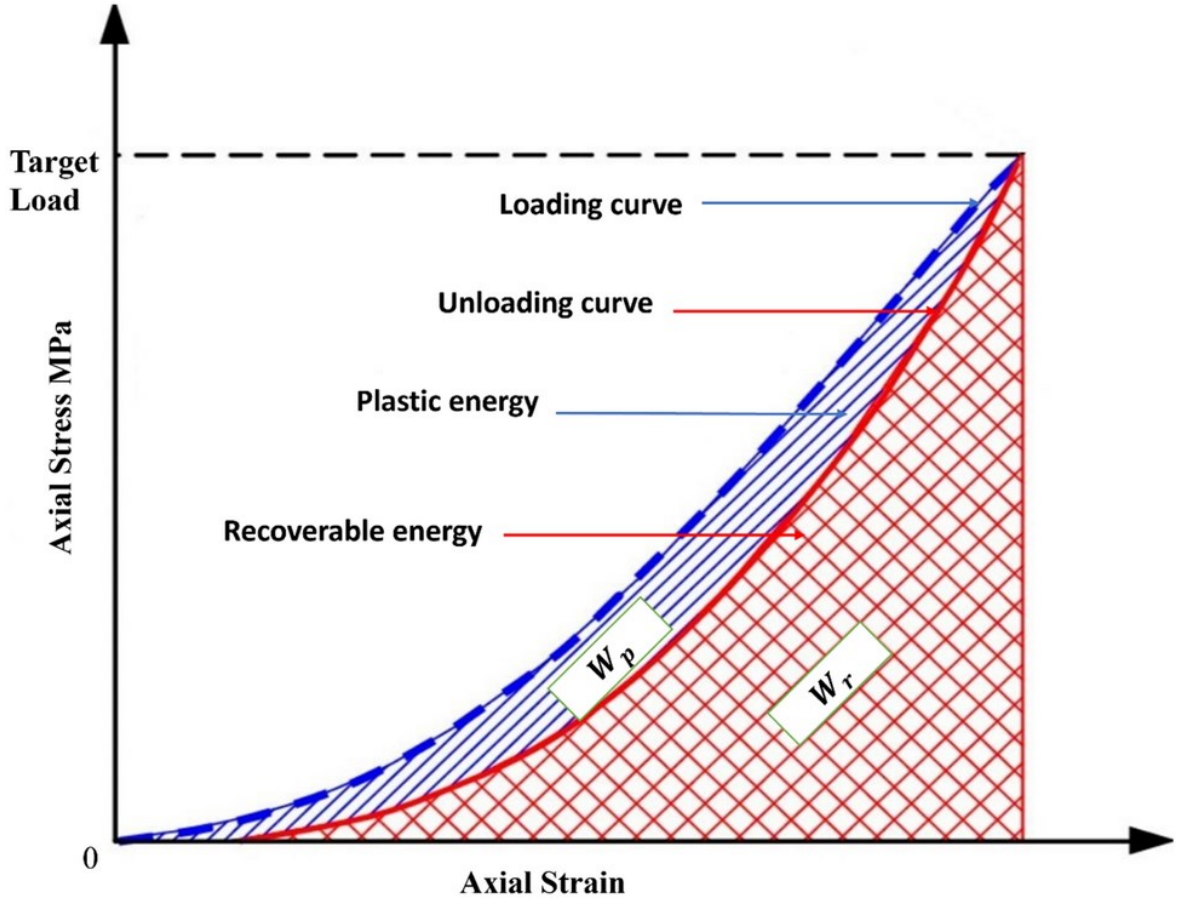

Figure 2.1: Energy components in a load-unload test (Malki et al., 2024).

Table 2.2: Classification of the W_{et} index for coal (Kidybinski, 1981).

W_{et}	Bursting level	Commentary
≥ 5	High	Fails in violent and dynamic mode with a broad spread of chips
5 > W_{et} > 2	Low	Intermediate failure behaviour
< 2	None	Quiet brittle fragmentation

2.2.2 Brittleness Index

Brittleness is another important factor to take into consideration which is tightly related to rockburst events. It can be defined as a property of the solid material that ruptures with little or no ductile deformation (Bates and Jackson, 1984). Peng et al. (1996) defined brittleness, B, as the ratio of the unconfined compressive strength (σ_c) to the tensile strength (σ_t) as follows.

$$B = \frac{\sigma_c}{\sigma_t} \tag{2.2}$$

As part of their work, they proposed a range of values which relate the B value to the potential rockburst level. These ranges are listed in Table 2.3. As can be seen, strong burstability is associated with $B \leq 14.5$. However, Li et al. (2001) proposed an entirely different range of brittleness ratios as shown in Table 2.3. The suggested trend is in contrast with that of Peng et al. (1996) with $B > 18$ for strong burstability. Finally, Zhang et al. (2011) suggested a slightly different range B values while following a similar trend to that of Li et al. (2001) as shown in Table 2.3. These inconsistencies suggest that the Brittleness Index may not be suitable criterion as a congruent rock burstability criterion as not only the B value ranges are different but more importantly the trends are contrasting.

Table 2.3: Brittleness ratio (Peng et al., 1996, Li et al., 2001, Zhang et al., 2011).

Rockburst level	B (Peng et al., 1996)	B(Li et al., 2001)	B(Zhang et al., 2011)
None	$B > 40$	$B < 10$	$B < 15$
Weak	$26.7 < B \leq 26.7$	-	$15 < B < 18$
Medium	$14.5 < B \leq 26.7$	$10 \leq B \leq 18$	$18 < B < 22$
Strong	$B \leq 14.5$	$B > 18$	$B \geq 22$

2.2.3 Strain Energy Density Index (SED)

Wang and Park (2001) suggested the use of elastic strain energy density similar to Strain Energy Storage index but considering a uniform state of stress in a rock sample. This index is defined by the information obtained from a uniaxial compression strength (UCS) test namely the peak strength, σ_c, and the unloading tangential modulus, (E_s) as follows.

$$SED = \frac{\sigma_c^2}{2E_s} \tag{2.3}$$

The suggested ranges for rockburst hazard based on SED value are listed in Table 2.4. As can be seen, an SED value > 200 is indicative of highly burstable rock material.

Table 2.4: SED values proposed by Wang and Park (2001).

SED value (KJ/m^3)	Rockburst hazard
SED ≤ 50	Very low
50 < SED ≤ 100	Low
100 < SED ≤ 150	Moderate

$150 < SED \leq 200$	High
$SED > 200$	Very high

Cai (2016) proposed slightly different ranges for SED linked to four levels of rockburst hazard namely weak, medium, strong, and very strong. His suggestion for very strong burstability of SED > 200 is identical to that of Wang and Park (2001). Given the consistency between the two studies, equation 2.3 will be used in this study to calculate SED and assess rock burstability.

Table 2.5: SED values proposed by Cai (2016) and its rockburst hazard.

SED value (KJ/m^3)	Rockburst hazard
$SED < 40$	Weak
$40 < SED \leq 100$	Medium
$100 < SED \leq 200$	Strong
$SED > 200$	Very Strong

2.3 Rockburst prediction due to geologic parameters

Geological structures have been reported as an important factor by many researchers impacting rockburst occurrence (Lu et al., 2018, He et al., 2018). These structures can be either small local structures like foliations and local damage zones, or large-scale like faults and dykes which can range from 100 m to more than 1000 m and even be at a regional scale of several kilometers. Small scale structures tend to be detrimental for certain civil engineering tunnels like in the construction of the civil tunnel Jinping-II (Zhou et al., 2015). Large-scale structures tend to be associated with mining operations; these major structures can affect the rockmass behaviour by creating an unfavorable stress state with the structures having different properties from the host rockmass.

This difference of values in their properties could result in stress concentration allowing rockburst to occur. An example of this issue took place in Strathcona, Canada where an event occurred due to the difference in the material properties of an intrusive diabase dyke and the host rock (Blake and Hedley, 2009). Another well studied case occurred in Mount Charlotte, Australia where large wedges formed by two intersecting faults enabled large shear movements with a massive release of seismic energy (Mikula and Lee, 2002). Most events which occurred far from the mining area are dominated by the large-scale interaction which can happen between geological structures (Bewick et al., 2009).

Overall, the presence of geological structures may range from sliding behavior along geological discontinuities which were pre-existing to stress re-distribution due to the creation of new fault surfaces and its interaction with other geological structures. The effect of such geologic parameters adds to the stress concentration and can result in rockbursts after nearby production blasting has taken place.

Faults are a specific case of geological structures tightly related to rockburst; they are recognized as a major controlling factor which contributes to the occurrence of large magnitude rockburst events (Durrheim et al., 1998). It is important to understand the properties of the fault as they may affect rock bursting events. The extent, relative position to the excavation, and orientation of the fault are important factors for the occurrence of rockbursts (Manouchehrian and Cai, 2018). Even though the effects of the geological structures and other geologic parameters are well-stablished in the literature, they are mainly qualitative and there are no criteria for rockburst prediction based on the geologic parameters.

2.4 Rockburst prediction due to mining conditions

Many underground mines report the occurrence of intense and frequent seismic activities. This is particularly true in hard rock mines employing extraction methods that lead to stress buildup in secondary blocks in primary-secondary mining systems, which in turn cause large seismic events and rockburst damage. This type of rockburst is attributed mainly to the changes in the mining geometry with time because of stope extraction in a planned sequence. The most widely used tool for the prediction of mine geometric burstability based on mining-induced stresses is numerical modelling. Numerical methods and techniques related to computing are nowadays important tools to assess engineering and scientific challenges which were not possible to handle before (Gu, 2013).

While well-known rock failure criteria such as Mohr-Coulomb (Jaeger and Cook, 1979) and Hoek-Brown (Hoek et al., 2002) are used to examine the rockmass stability condition and failure due to yielding, they are not particularly suited to examine burst potential due to mine geometric parameters. There are two main indices that are particularly used as criteria for determining rock bursting proneness due to mining induced stress. They are the Burst Potential Index (BPI) (Mitri et al., 1999) and the Brittle Shear Ratio (BSR) (Castro et al., 2012). These are presented below.

2.4.1 Burst Potential Index

The Burst Potential Index (BPI) was first proposed to allow for the calculation of mining-induced strain energy stored in the rock mass (Mitri et al., 1999). Using the results of uniaxial compression test, the critical energy density, e_c, is calculated. The energy storage rate, ESR, is calculated from the numerical modelling results; it is defined as the energy storage rate per unit volume of the rock due to mining. Figure 2.2 (Mitri et al., 1999) illustrates the mining induced stress, σ_A, and the energy component associated with it. As can be seen in Figure 2.2, ESR is defined by the area under the stress-strain curve between the in-situ stress, σ_0, and induced stress, σ_A. The calculations are as follows.

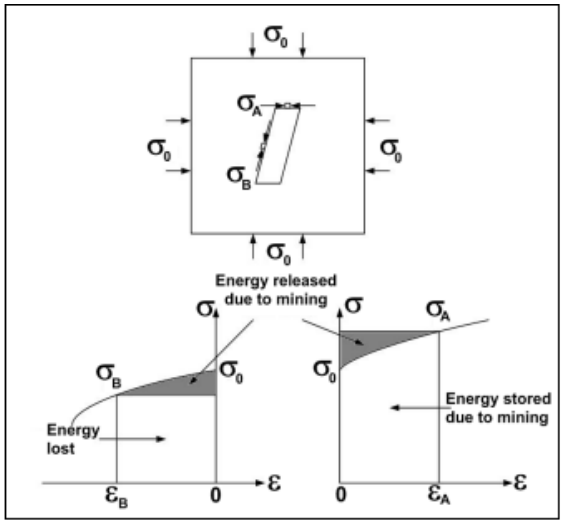

Figure 2.2: Mining-induced stress and its energy component (Mitri et al., 1999).

$$ESR = \int_0^{\varepsilon_A} \sigma d\varepsilon \tag{2.4}$$

Another parameter that is needed to calculate BPI is the critical energy density value, e_c. It is defined as the area under the stress-strain curve up to the peak stress value of stress. It is given by the integral with respect to the uniaxial peak strain, ε_P.

$$e_c = \int_0^{\varepsilon_P} \sigma d\varepsilon \tag{2.5}$$

Finally, the BPI is calculated from

$$BPI = \frac{ESR}{e_c} 100\% \tag{2.6}$$

The above equation is valid for 2-dimensional analyses only, whereby the quantity, e_c, can be estimated from the results of a uniaxial compressive strength. For 3-D analysis, the strain energy capacity of the rock will depend on the confinement stress, σ_3. Also, ESR will depend on the state of stress σ_1, σ_3. Khalil (2023) defined the ESR in 3-D by the following expression.

$$ESR = \int \{\sigma\}\, d\varepsilon = \frac{1}{2}\{\varepsilon\}^T [D]\{\varepsilon\} + \{\varepsilon\}^T \{\sigma^o\} \tag{2.7}$$

Where $\{\sigma\}$ and $\{\varepsilon\}$ are the induced stress and strain vectors, $\{\sigma^o\}$ is the in-situ stress vector, and [D] is the elasticity matrix. The advantage of the BPI as a burst indicator is that it depends on the coupled effect of stress and stiffness or strain (Mitri, 2007).

For 3D applications, Vennes et al. (2020) proposed to calculate the critical strain energy density using Hoek-Brown criterion. The rock strength under triaxial loading condition is estimated as the peak principal stress, σ_1^{peak} for a given σ_3 is calculated as follows:

$$\sigma_1^{peak} = \sigma_3 + \sigma_{ci}\left[m_b \frac{\sigma_3}{\sigma_{ci}} + s\right]^a \tag{2.8}$$

Where σ_{ci} is the uniaxial compressive strength of the intact rock material and $m_b, s,$ and a are material constants. Then, Hooke's law is applied to determine the principal strains at failure under triaxial loading, considering that $\sigma_{11} = \sigma_1$, $\sigma_{12} = \sigma_{23} = \sigma_{13} = 0$, and $\sigma_{22} = \sigma_{33} = \sigma_r$. The critical strain energy of the rock under triaxial conditions is given by

$$e_c = \frac{1}{2}(\sigma_1, \sigma_3, \sigma_3)^T(\varepsilon_1, \varepsilon_3, \varepsilon_3) = \frac{1}{2E}\left(\sigma_1^{peak\,2} + 2\sigma_3^2 - 2\upsilon\left(2\sigma_1^{peak}\sigma_3 + \sigma_3^2\right)\right) \tag{2.9}$$

2.4.2 Brittle Shear Ratio

The Brittle Shear Ratio (BSR) is a common index used nowadays to assess the rock burstability Castro et al. (2012). It uses the ratio of the deviatoric stress to the UCS value to assess burst potential. A set of ranges for the ratio are proposed by Castro et al. (2012) as shown in Table 2.6. The formula for the BSR is as follows.

$$BSR = \frac{\sigma_1 - \sigma_3}{\sigma_c} \tag{2.10}$$

Where σ_1 is the principal major stress, σ_3 is the principal minor stress and σ_c is the UCS value. One important consideration is that loading stiffness is not measured by the BSR index.

Table 2.6: Rockmass damage and potential for strainburst based on BSR (Castro et al., 2012).

BSR	Rock Mass Damage	Strainburst potential
0.35	No to minor	No
0.35 to 0.45	Minor (surface spalling is a potential case)	No
0.45 to 0.6	Moderate (breakout formation can be expected)	Minor
0.6 to 0.7	Moderate to Major	Moderate
> 0.7	Major	Major

2.5 Summary

To summarize, based on the four causes for rockburst, which were identified, there has been a lot of research on the characterization and prediction of rockburst potential with geotechnical parameters with many criteria developed over the years such as SED, B, and BSR. While geologic parameters play an important role in the creation of rockburst events, it is often quite challenging

to measure the exact impact of the presence of geological structures on rockburst events, thus making these parameters important but not necessarily easy to categorize in a formula. Mining parameters, on the other hand, are controllable to a certain degree as the decisions on backfill material selection, mining sequence, and sizes of the stopes can be engineered. It is possible that rockburst can be triggered due to mining sequences and this can greatly affect the performance of a mining operation. There is plenty of evidence where the rock materials do not meet burstability criteria yet a rockburst occurs. This may suggest that the geometric parameters may be the most relevant driver in this case. The focus of this research will be set on suggesting ways to better understand the effect of mining geometry on mining-induced seismicity. To better support it, numerical modelling will be used as it is a useful tool to assess stability and to reproduce the complex conditions inherent to the underground mines.

As rockbursts are naturally induced by excavation activities such as mining and tunnelling, such factor is considered essential for rockbursts to occur. Likewise, microseismic activities are a natural companion to rockburst occurrence, therefore, they are not considered as an independent cause for rockburst. Rather, they are dependent on excavation activities. In this study, the following classification of independent rockburst causes is proposed as follows.

1. Rock mechanics properties (SED, W_{et}, brittleness, etc.)
2. Geological structures (faults, dykes, shear zones, etc.)
3. Mine geometry (mining method, stope dimensions, mining sequence, sill pillars, in-situ stress (depth), etc.)

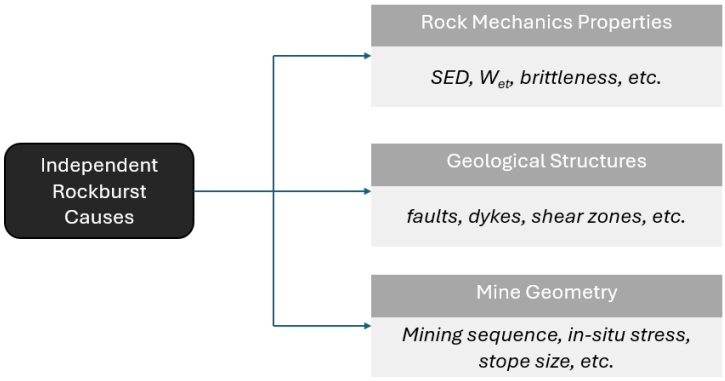

Figure 2.3: Flowchart of independent rockburst causes.

Bridging text between manuscripts

The following chapter reports on a case study of Macassa Mine of Agnico Eagle Ltd. in northern Ontario, Canada. The evaluated case is of a sill pillar situated 5,600 feet (1,700 m) below surface. It is 360 feet (110 m) long and 50 feet (15.5 m) in height, with a varying thickness averaging 3 m. The sill pillar is planned for extraction with longhole stoping in retreat. Past mining activities employed cut-and-fill methods. The levels above and below the sill pillar are tight filled with pastefill. To assess the stress condition in the pillar, a 3D mine wide numerical model was created with FLAC3D finite difference code. The numerical model employs the Macassa geomechanical database and in-situ stress regime. Pillar burst conditions are assessed using the deviatoric stress ratio, also known as the brittle shear ratio (BSR), to estimate potential brittle shear failure, and the burst potential index (BPI) based on energy considerations to examine strainburst potential. Model calibration relied on microseismic monitoring activities in the sill pillar over the past year. Rockburst mitigation and control methods with dynamic support in the sill drives are discussed.

The chapter is a peer-reviewed paper that appeared in Proceedings of the 10th International Conference on Deep and High Stress Mining, pp. 659-672. The conference was held in Montreal in August 2024. The Proceedings are published by the Australian Centre for Geomechanics, Perth. This research article is available at: https://doi.org/10.36487/ACG_repo/2465_40

Chapter 3 – Rockburst assessment in the recovery of a deep sill pillar in Macassa Mine

3.1 Abstract

Rockburst control in deep mining is a challenging problem, especially in high extraction ratio zones. The increased likelihood of rockburst occurrence can be a cause of safety concerns for the mine operators. The parameters associated with rockbursts are generally related to geological features, rock properties, seismic activities and the mining rate. Mining aspects such as mining sequence, mining direction, stope geometry, backfill selection and the mining method all contribute to the occurrence of rockburst. This study demonstrates a stepwise methodology for the assessment and safe recovery of a sill pillar at Agnico Eagle Mines Ltd's Macassa mine. The pillar is situated 1,700 m (5,600 ft) below surface. It is 110 m (360 ft) long and 15.5 m (50 ft) in height, with a varying thickness averaging 3 m (10 ft). The sill pillar is planned for extraction with longhole stoping in retreat. Past mining activities employed the cut-and-fill method; the levels above and below the sill pillar are tight-filled with paste fill. To assess the stress condition in the pillar, a 3D mine-wide numerical model was created with FLAC3D finite difference code. The numerical model employs the Macassa geomechanical database and in situ stress regime. Pillar burst conditions are assessed using the deviatoric stress ratio to estimate potential brittle shear failure, and the burst potential index based on energy considerations to examine strainburst potential. Model calibration relies on microseismic monitoring activities in the sill pillar over the past year. Rockburst mitigation and control methods with dynamic supports in the sill drives are discussed.

3.2 Introduction

Based on recent research, various authors have linked rockbursts to energy release (Blake, 1972; Gill et al., 1993; He et al., 2007), brittle rock properties (He, 2005; Solak, 2009), and seismic activities (Hedley, 1992; Blake and Hedley, 2003). A critical aspect in understanding and assessing rockburst lies in its classification, which captures pertinent information about these occurrences. Various classification systems have been proposed with a variety of properties to represent the different types of events which occur underground.

Kaiser et al. (1996) based their classification on the types of rockburst damage mechanism and damage severity. He et al. (2012) reported a classification defined by the triggering mechanism with the support of laboratory data. They based their classification on a series of tests simulating the conditions in deep mining. The early classification proposed by Ortlepp (1992) is the first one to relate the seismic event type to the source mechanism, first motion seismic records, and event magnitude; see Table 3.1.

Table 3.1: Classification of rockburst types proposed by Ortlepp (1992).

Seismic Event	**Postulated Source Mechanism**	**First Motion Seismic Records**	**Ritcher Magnitude M_L**
Strain Bursting	Superficial spalling with violent ejections of fragments	Usually undetected, could be implosive	-0.2 to 0
Buckling	Outward expulsion of larger slabs pre-existing parallel to opening	Implosive	0 to +1.5
Pillar or face crush	Violent expulsion of rock from tunnel face or pillar	Implosive	+1.0 to +2.5
Shear rupture	Violent propagation of shear fracture through intact rock mass	Double-couple shear	+2.0 to +3.5
Fault-slip	Violent renewed movement on existing fault	Double-couple shear	+2.5 to +5.0

Another relevant topic to address regarding rockbursts are their causes. Kaiser and Cai (2018) proposed to categorize the causes for rockbursts into 4 main groups: geotechnical, geologic, mining, and seismic-related parameters. However, it can be argued that seismic activities are a natural companion to rockburst occurrence, thus, they cannot be defined as an independent cause for rockburst events. Therefore, leaving aside the events which occur because of natural seismicity, the primary cause for rockburst events is mining with geological and geotechnical factors influencing the severity of a rockburst event.

3.2.1 Brittle shear ratio

The Brittle Shear Ratio (BSR) is an index used in the mining industry as a tool to assess rock burstability. It was defined by Castro et al. (2012) as a means to determine the rock mass damage and its relation to potential occurrence of strain bursting by using the difference between the major

and minor principal stress and its relationship with the UCS value as it can be seen in the Formula 3.1.

$$BSR = \frac{\sigma_1 - \sigma_3}{\sigma_c} \quad (3.1)$$

where:

σ_1 = Major Principal Stress Value

σ_3 = Minor Principal Stress Value

σ_c = Uniaxial Compressive Strength Value.

The relationship between BSR and rockburst events is established in the Table 3.2.

Table 3.2: Relation between value of BSR, rock mass damage and its potential regarding strain bursting (Castro et al., 2012).

BSR	**Rock mass damage**	**Potential for strain bursting**
0.35	No to minor	No
0.35 to 0.45	Minor (surface spalling is a potential case)	No
0.45 to 0.6	Moderate (breakout formation expected)	Minor
0.6 to 0.7	Moderate to Major	Moderate
> 0.7	Major	Major

3.2.2 Burst potential index

The Burst Potential Index (BPI) is a parameter which describes the ratio between the strain energy stored due to mining and the critical strain energy density value. At first, it was defined as a 2D application which considered the mining induced stresses, and the energy components related to it (Mitri et al., 1999). Equation 3.2 shows the calculation of BPI. Khalil (2023) defined a formula to calculate the value of the parameters for a 3-D analysis where the strain energy of the rock will depend on the confinement stress (σ_3) and the energy parameter will depend on the state of both the peak principal stress (σ_1) and the confinement stress (σ_3). These equations are shown in Equations 3.3, 3.4 and 3.5.

$$BPI = \frac{ESR}{e_c} \quad (3.2)$$

where:

ESR = Energy storage rate, it refers to the strain energy stored due to mining in a stress-strain curve.

e_c = Critical strain energy density value

For the calculation of the energy storage rate, a formula proposed by Vennes et al. (2020) which accounts for the total Energy storage rate is presented (equation 3.3).

$$ESR_i = 0.5 * \{\sigma_{prin}\}^T_i * \{\varepsilon_{prin}\}_i \quad (3.3)$$

where:

ε_{prin} = Principal strain vector

σ_{prin} = Principal stress vector

Equation 3.4 shows the calculation for the peak principal stress which is necessary to calculate the critical strain energy density value.

$$\sigma_1^{peak} = \sigma_3 + \sigma_{ci}\left[m_b \frac{\sigma_3}{\sigma_{ci}} + s\right]^a \quad (3.4)$$

where:

σ_1^{peak} = Peak principal stress

σ_3 = Minor principal stress

σ_{ci} = Uniaxial compressive stress of the intact rock

m_b, s, a = Material constants introduced for the generalized Hoek-Brown failure criterion (Hoek et al., 2002)

Equation 3.5 shows the calculation of the energy density value based on the peak principal stress.

$$e_c = \frac{1}{2E}\left(\sigma_1^{peak\,2} + 2\sigma_3^2 - 2\upsilon\left(2\sigma_1^{peak}\sigma_3 + \sigma_3^2\right)\right) \quad (3.5)$$

where:

E = Young modulus of the material

υ = Poisson's ratio of the material

In the case of BPI, a higher value means a greater potential of bursting.

This paper presents a stepwise methodology for the assessment and safe recovery of a sill pillar at Macassa Mine of Agnico Eagle Mines Ltd. To assess the stress condition in the pillar, an elastic 3D mine wide numerical model was created with the FLAC3D 7 software (Itasca, 2019). The numerical model employs the Macassa geomechanical database and in-situ stress regime. Pillar burst conditions are assessed using the deviatoric stress ratio to estimate potential brittle shear failure, and the Burst Potential Index based on strain energy considerations to examine strainburst potential.

To relate modelled stress conditions and burst prone rock mass conditions to support design, the design assessment must consider factors such as the varying susceptibility of excavations to damage, the different damage mechanisms, the interaction of the ground support schemes with the events, and the variability of the available data (Mikula, 2012). Dynamic support systems have three main parameters: energy absorption capacity, displacement capacity, and load capacity.

Ortlepp (1992) proposed an approach for design of support considering rockburst damage in tunnels. He used energy, tendons, the cladding elements, and extent of the yield as the main steps. In his considerations, the design principles are based on the ejection of a single block, closely related to strainbursts. Another approach was proposed as a result of the Canadian Rockburst research program (1996) after the CAMIRO mining division conducted research on Canadian rockburst events and how the support systems behaved. This approach defined three levels of damage from minor to major. Mikula (2012) developed an empirical chart for the selection of dynamic ground support based on the historical data available at Long-Victor Mine.

Based on the literature previously mentioned and other authors (McGarr, 1997, Varden et al., 2008), it is necessary to determine the wall damage due to the seismic activity and the related ejection velocity. A good measurement of these components is the energy related to the ejected particle. The kinetic energy considers both the ejection velocity of the particle, and the wall damage expressed in the mass of the kinetic energy formula as it was stablished by Guntumadugu (2013). Formula 3.6 shows the equation for the kinetic energy (K_e), the mass can be obtained from numerical modelling while the ejected velocity can be calculated based on the empirical data available from the mine.

$$Ke = \frac{1}{2} * m * v^2 \tag{3.6}$$

where:

m = Mass of the particle ejected

v = Velocity of the particle ejected

3.3 Case Study

The Macassa Mine is situated in the town of Kirkland Lake, Ontario, Canada (Figure 3.1) within the Abitibi Greenstone Belt. Since its discovery in 1933, Macassa has been a significant gold producer for the country. The operation was suspended in 1999 due to the low gold price but resumed operation in 2002 and later, in 2005, the discovery of the high-grade South Mine Complex (SMC) consolidated the operation.

The current average production rate is of 1,000 tonnes per day with the two main horizons being the historical Main Break and the SMC. The Main Break zone is dipping at 75°, while the SMC zone is shallower with a dip of 45°. The predominant mining methods used are overhand and underhand cut-and-fill, with some long hole bulk methods where the conditions are appropriate. All stopes are backfilled with the majority of the SMC backfilled using paste fill.

This study will consider the sill pillar located on the SMC. The pillar is situated 5,600 feet (1,700 m) below surface. It is 360 feet (110 m) in length and 50 feet (15.5 m) in height, with a varying thickness averaging 3 m. As seen in Figure 3.2, the sill pillar is surrounded by previously mined stopes which are currently backfilled. The main objective of this paper is to assess the stability condition and to support the design of a safe sill pillar recovery. The sill pillar will be extracted with long hole stoping in retreat. To assess the stress condition in the pillar, an elastic 3D mine-wide numerical model has been created with the FLAC3D software (Itasca, 2019). The numerical model was based upon the Macassa geomechanical database and in-situ stress regime evaluation. Pillar burst conditions were assessed using Brittle Shear Ratio, and the Burst Potential Index based on energy considerations. Model calibration relied upon microseismic monitoring activities in the sill pillar over the past year that demonstrated a stable state which should be reflected on the model to be considered as calibrated.

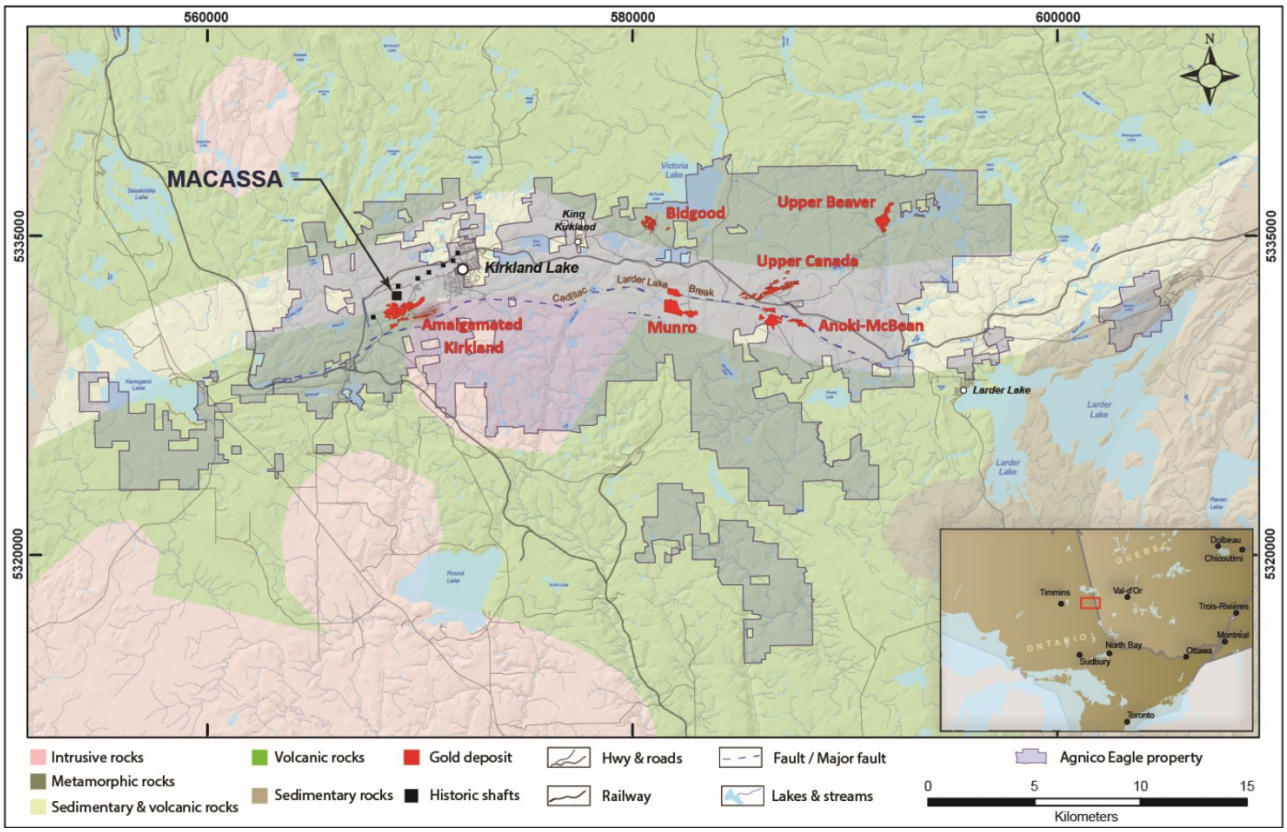

Figure 3.1: Kirkland Lake Camp – Property and Regional Geology Map, image from Agnico Eagle Mines Limited.

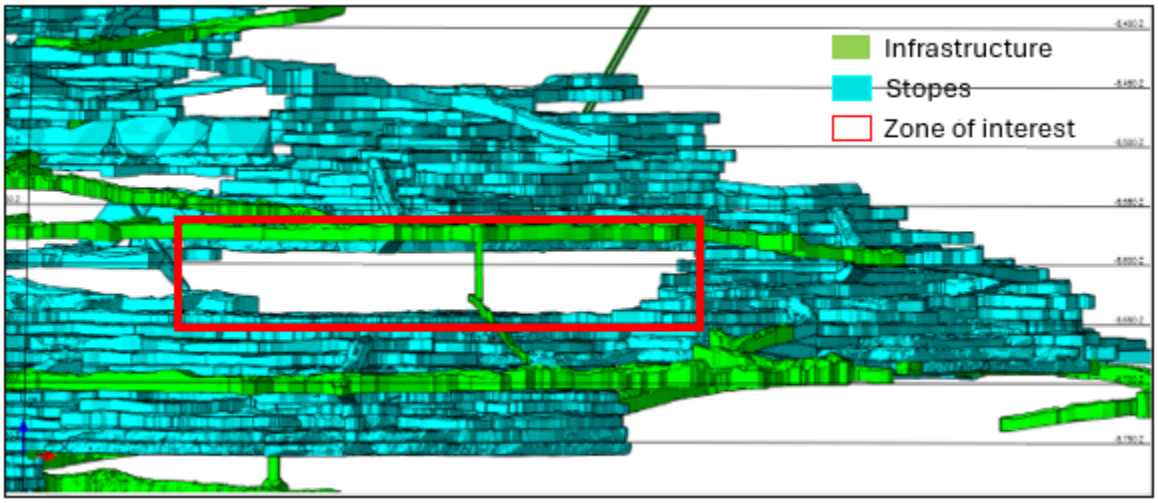

Figure 3.2: Sill pillar zone view, it is located in the South Mine Complex about 5600 feet in depth and it is surrounded by backfilled stopes.

3.4 Numerical Model

A mine-wide model was elaborated to better represent the stress state. The dimensions in each direction are at least 5 times the measures of the sill pillar considering the access and crosscuts related to its exploitation. These dimensions were chosen to assure that the stress state would confidently represent the current stress state of the mine. For this case, the dimensions of the sill pillar for the exploitation of the first 2 stopes of approximately 40 meters length and 20 meters in height are considered (Figure 3.3). The total dimension of the boundary box is assured to be more than 220 meters in the z direction and 880 meters in both x and y directions. Macassa is an interesting case from the perspective of modelling, since the stopes are of similar size to the infrastructure due to the main mining methods, being predominantly cut-and-fill. As a result, the effect of mine development is included in the model to measure the stress state.

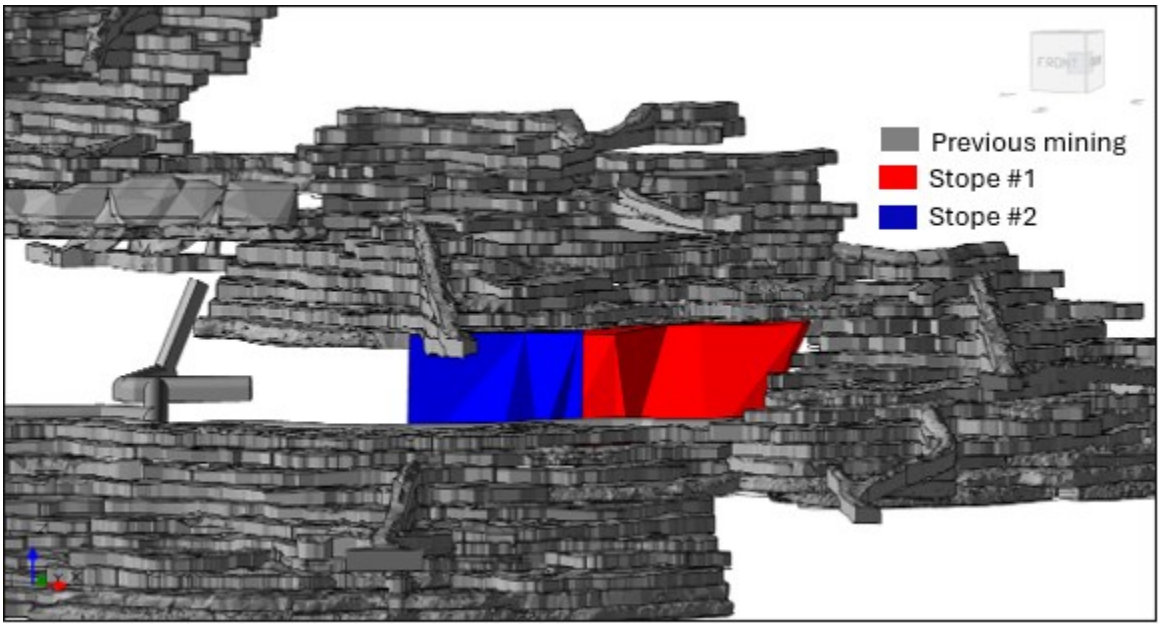

Figure 3.3: Front view of the Stopes located on the sill pillar.

For the elaboration of the model, it was necessary to define the parameters of its construction. With over 2.5 million zones defined, the zone sizes were adjusted depending on whether there were or not any excavation. When there was an excavation nearby, the size of the zone was minimized to 1 meter. Once the excavation was modelled, a zone of 5 meters from the excavation progressively increased its size up to 4 meters. Out of this space, all the intact zone was modelled to be 8 meters.

The grid is composed by cubes of 1 m x 1 m x 1 m dimensions. Where there is a change in the lithology, the cubes were split into smaller cubes to assure the proper classification for the material distribution. Figure 3.4 shows the different lithologies which were used to represent the distribution of the material properties in the mine, those were based on the latest information provided by the mine. The main properties of the materials are shown in Table 3.3.

A gravity field stress was assumed and roller boundaries for the horizontal constrains were assumed for the kinematic boundary conditions. A model gravity of 9.8 m/s^2 was assumed but due to the different specific densities, there was not a uniform distribution of the stress in the vertical direction. For the direction of the principal stress, based on empirical observations made throughout the mine, the major principal stress is assumed to be horizontal and perpendicular to the strike of the structure. In this case, the direction of the major principal stress is N45°E.

Six (6) lithologies with different properties have been identified at Macassa. The predominant lithology within the sill pillar is syenite porphyry.

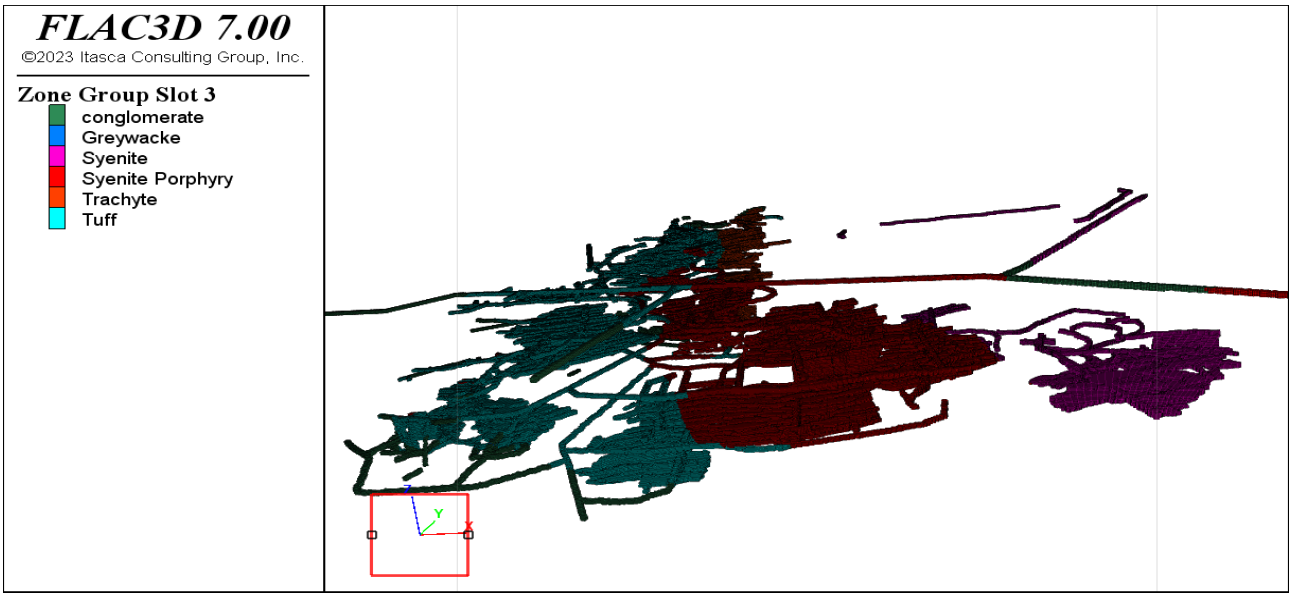

Figure 3.4: Lithologies available at the zone of the sill pillar.

Table 3.3: Properties of the lithologies of the sill pillar zone used for numerical modelling.

Lithology	UCS (MPa)	Density (g/cm^3)	Young's Modulus (GPa)	Poisson's ratio
Syenite Porphyry	114	2.7	68	0.26
Tuff	154	2.8	72	0.23
Basic Syenite	210	2.9	74	0.30
Trachyte	163	2.7	67	0.24
Conglomerate	132	2.7	67	0.24
Greywacke	158	2.7	70	0.26

For the modelling exercise, the mining sequence was represented by a sequence of steps where the stress state within the sill pillar was estimated. Model Steps 1 through 9 represent the formation of the sill pillar. Model Steps 10 through 11 represent sill pillar mining, with Step 10 modelling undercut development, and Step 11 modelling excavation of the first long hole stope. Stability evaluation of Steps 9 through 11 were evaluated with BSR and BPI.

Observations from the field were used to calibrate the model. In Step 9, a stable state of the sill pillar prior to stope extraction is demonstrated by BSR values in the core of pillar below 0.6, indicating minor rock mass damage with no strainburst potential, as per Castro et al. (2012).

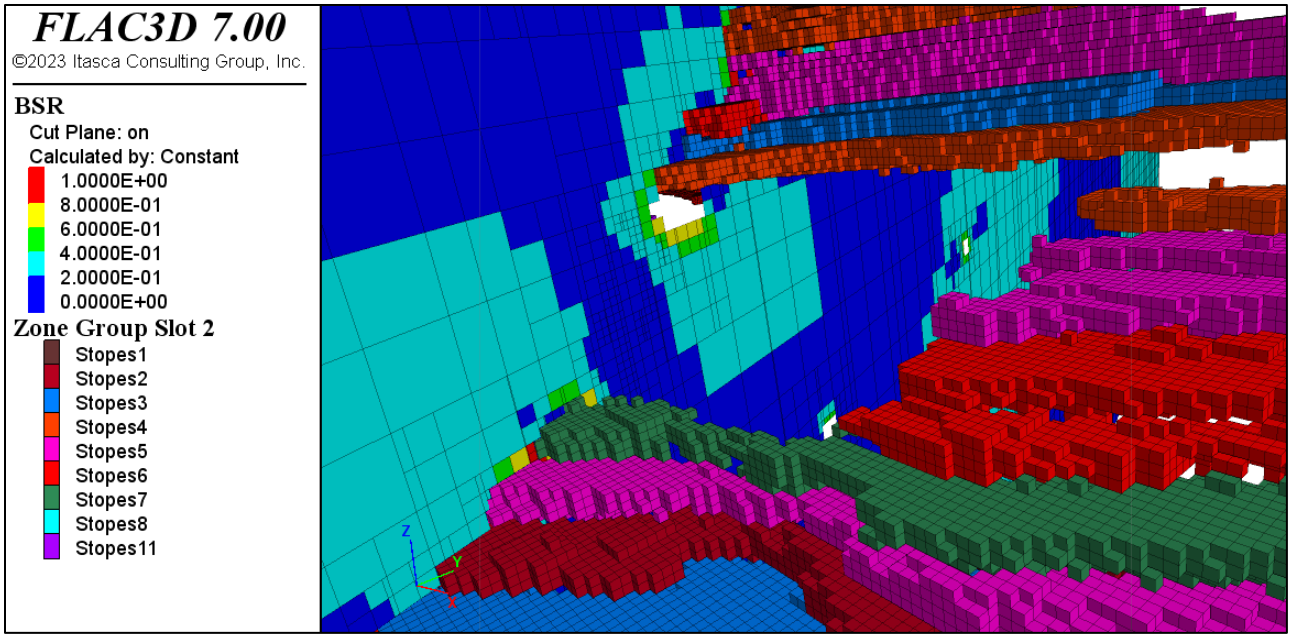

Figure 3.5: Sill pillar mining sequence geometries as constructed in FLAC3D, the plane shows the BSR values for Step 11.

3.5 Discussion of results

The pre-sill pillar mining stress state was evaluated in Step 9. Figure 3.6 shows a BSR plot (UCS 234 MPa) of the sill pillar cross section and illustrates the core of the pillar which has a BSR index of 0.2-0.3. According to Castro et al. (2012), a BSR of 0.2-0.3 should correspond to minor rock mass damage and minimal risk of strain bursting. The BPI plot in Figure 3.7 corresponds with a BPI index of 0-0.1, indicating the core of the pillar is not prone to strain bursting.

BPI was calculated through post processing due to prolonged computation process. Mb, s and a have been determined via various iterations by matching the “heat map” (BPI > 0.2 from previous events) with observed seismicity of the development.

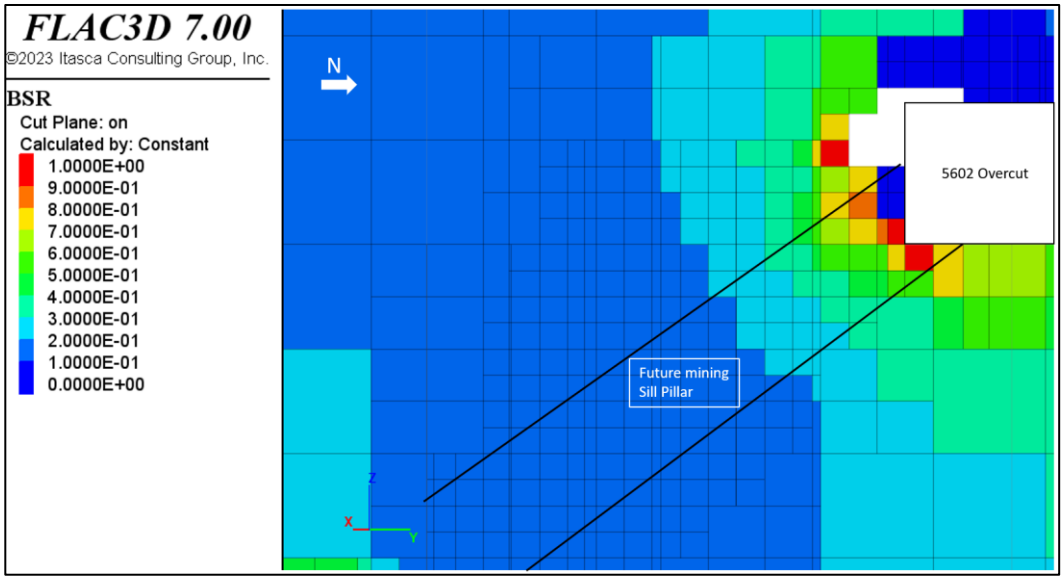

Figure 3.6: Sill pillar representative cross section displaying BSR plot, pre-sill pillar mining Step 9.

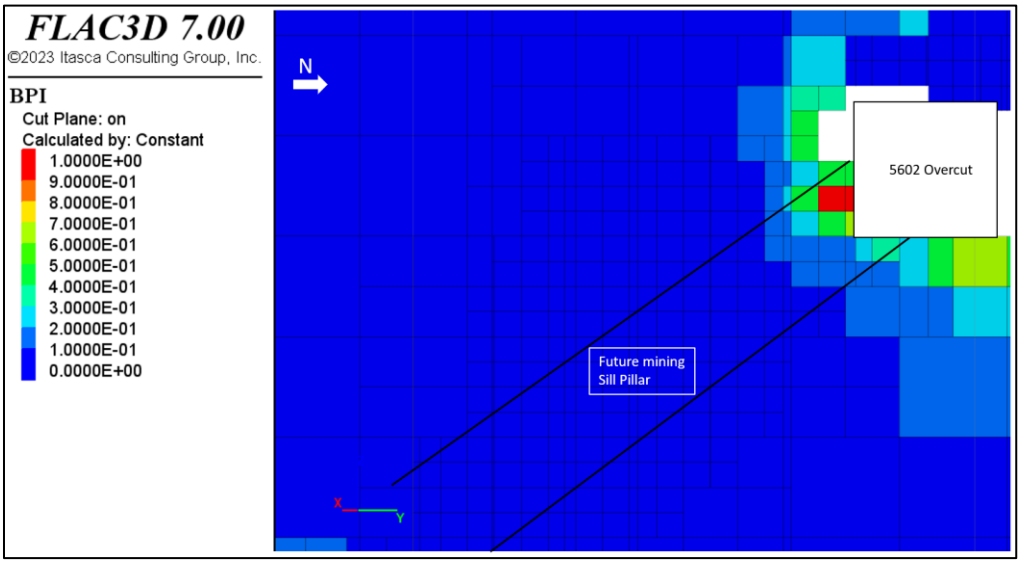

Figure 3.7: Sill pillar representative cross section displaying BPI plot, pre-sill pillar mining Step 9.

Observations from mining 5602 overcut concur with the model results. Seismicity was detected in the immediate rock mass surrounding development blasts and minimal seismic events were detected in the core of the pillar. Crews were able to install resin paddle bolts in the back and south wall with some difficulty. Minor seismic shakedown was experienced in the lower south walls following larger moment magnitude events greater than Mw 0. This damage correlates with the BSR values modelled to be greater than 0.5 surrounding the overcut, indicating moderate damage

to the rock mass and burst prone conditions. Long hole drilling through the core of the pillar has only triggered few, low magnitude seismicity around the collars and toes of the holes. No hole squeezing or crushing has been reported. Harder than usual rock was reported, prompting more frequent bit changes.

The pre-mining stress state was also evaluated at 50% strength of the average strength to determine BSR sensitivity to UCS values in case of varying rock mass strength along the sill pillar. Changing the UCS to 114 MPa, the BSR index for the core of the sill pillar plots at 0.3-0.4, as seen in Figure 3.8. This BSR range is still within the Castro et al. (2012) minor rock mass damage rating.

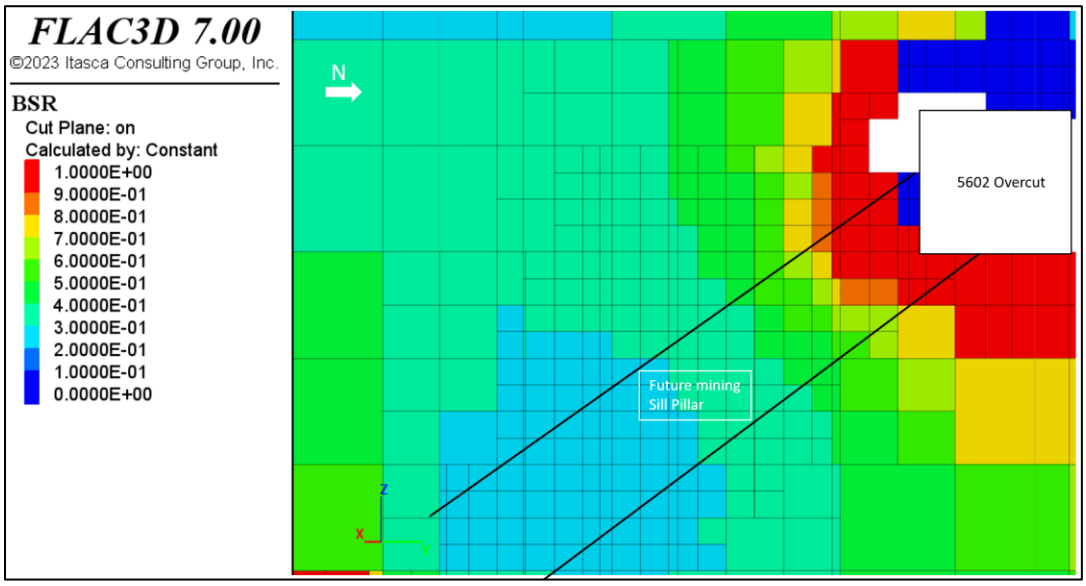

Figure 3.8: Sill pillar representative cross section displaying BSR plot for pre-sill pillar mining Step 9 at 50% UCS strength compared to UCS value used in calibrated model.

Both the BSR and BPI plots at Step 9, with varying UCS from 114 -234 MPa, demonstrate the model calibration for a stable pre-mining sill pillar stress state was achieved. Seismic data and underground observations from development and drilling confirm rock mass conditions are aligned with the BSR and BPI indexes. However, rock mass deformation over time and the resulting stress changes may not be adequately captured by an elastic model. It is necessary to understand how a deteriorating rock mass might change seismic response that will not be captured by an elastic model. As mining induced activities, such as blasting, changes the stress regime, we can expect increased seismicity in the remaining sill pillar to deteriorate the rock mass, increasing the BSR and BPI indexes and in turn, increasing the burst potential. A recommendation for future research

is to build an elastic-plastic model which will manage to more accurately represent the stress changes expected from rock mass deformation induced by stope blasting.

In Step 10, the stress state of the sill pillar was evaluated when developing the 5702 undercut using BSR and BPI indexes. The Figure 3.9 shows a BSR plot (UCS 234 MPa) of the sill pillar cross section. The sill pillar rock mass has progressed into the 0.3-0.4 range, and the intact core, with a BSR of 0.2-0.3, has been reduced. The Figure 3.10 BPI plot illustrates a range of 0-0.1, indicating low strain bursting potential.

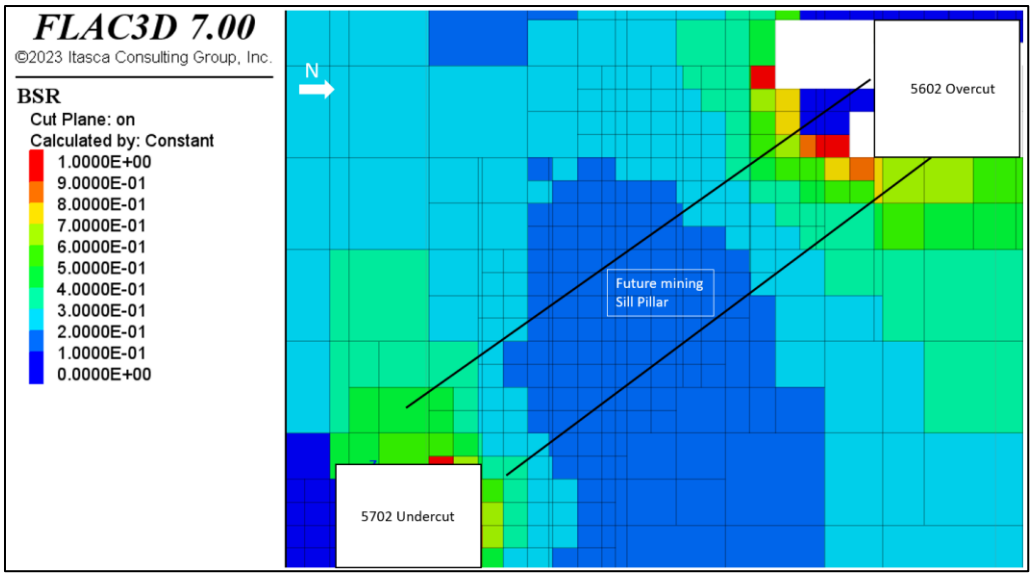

Figure 3.9: Sill pillar representative cross section displaying BSR plot for pre-sill pillar mining Step 10.

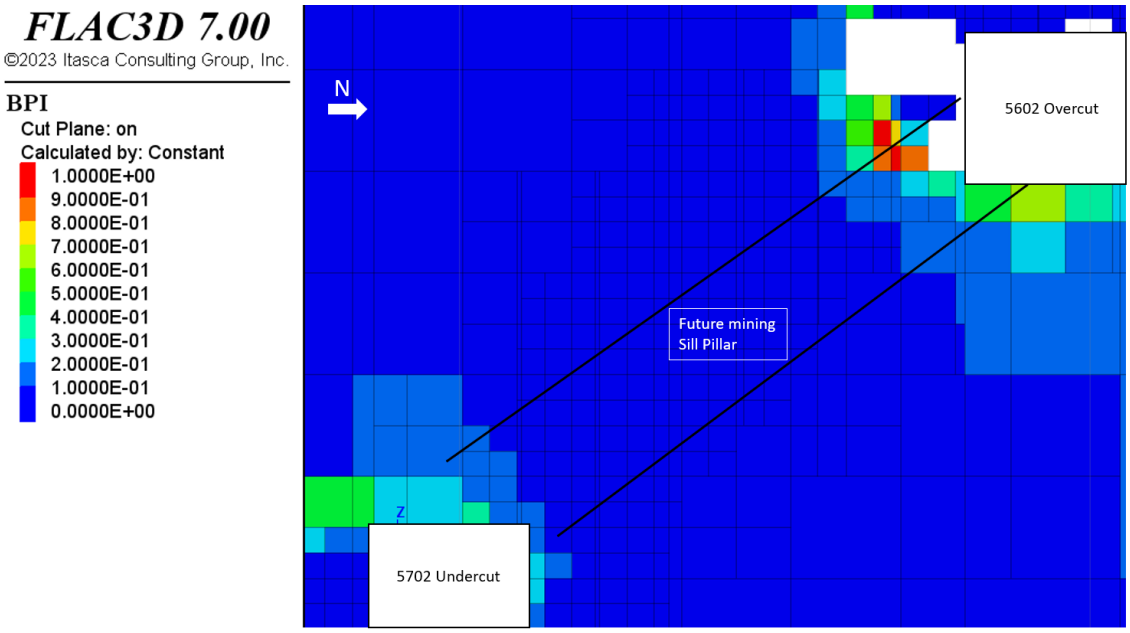

Figure 3.10: Sill pillar representative cross section displaying BPI plot for pre-sill pillar mining Step 10.

Observations from the undercut concur with the model results. Seismicity triggered by mining and blasting activities was detected in the immediate rock mass surrounding development blasts and minimal seismic events were detected in the core of the pillar. Crews were able to install resin paddle bolts in the back but were not able to install resin bolts in the north wall as the rock mass in the immediate 1-2m surrounding the excavation has spalled and deteriorated into gravel-like conditions due to the increased induced mining stresses. Elevated post blast seismicity with seismic events greater than Mw 0 characterize the seismicity response and stress state of the undercut.

In Step 11, the first sill pillar stope is extracted. Modelled BSR and BPI values indicate the stresses have been redistributed into the adjacent sill pillar longhole stope block, as seen in Figure 3.11. The intact core of the remaining sill pillar has been reduced significantly and the remaining pillar has a BSR greater than 0.5 and a BPI over 0.3, indicating Stope 2 mining activities, such as drilling and blasting, will be more likely to be exposed to burst prone conditions and seismicity will likely be detected throughout the entire pillar rather than just in the immediate rock mass surrounding the excavations.

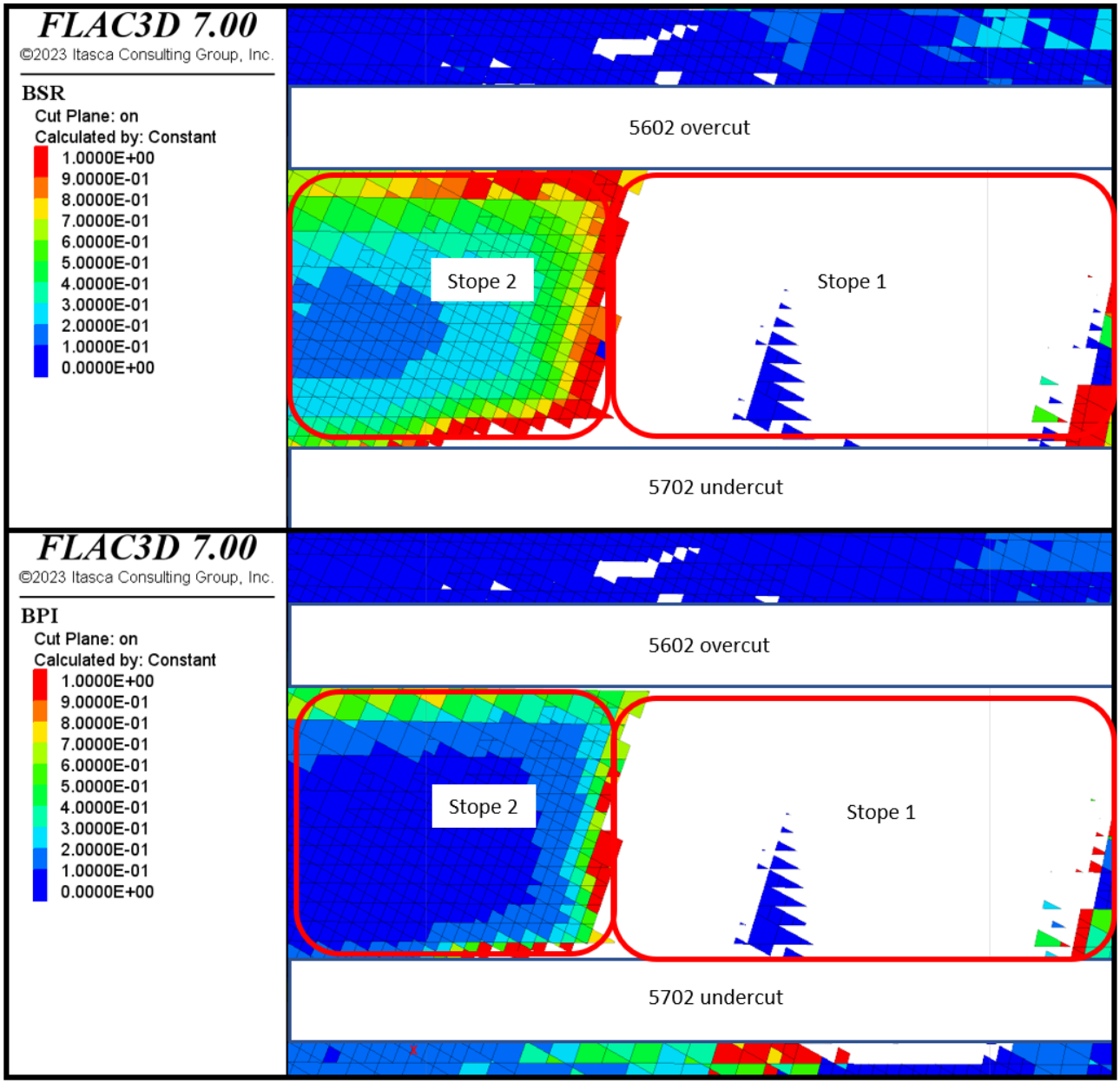

Figure 3.11: Sill pillar long sections displaying BSR and BPI plots for post Stope 1 blasting mining Step 11.

Using the calculated kinetic energy for strainbursts, dynamic support systems can be evaluated against anticipated stress and strainburst conditions. A review of seismic data for the sill pillar area determined the highest value of velocity for an ejected particle is below 1 m/s. Figure 3.12 illustrates larger magnitude events and their distance from the excavation that was recorded when mining development undercut. These large events were used in particle velocity calculations. For the purposes of conservative energy calculations, a value of 1.5 m/s, obtained from the mine

database, was assumed to be the critical case. The value of the mass was defined by setting a BSR index threshold of 0.6. For this sill pillar, a threshold BSR value of 0.6 is an appropriate assumption due to the increased likelihood for strain bursting as demonstrated by the model and observed during mining the overcut and undercut. Using Formula 3.6 for kinetic energy, a value of 16 KJ/m^2 was calculated to be the dynamic load applied to the ground support system.

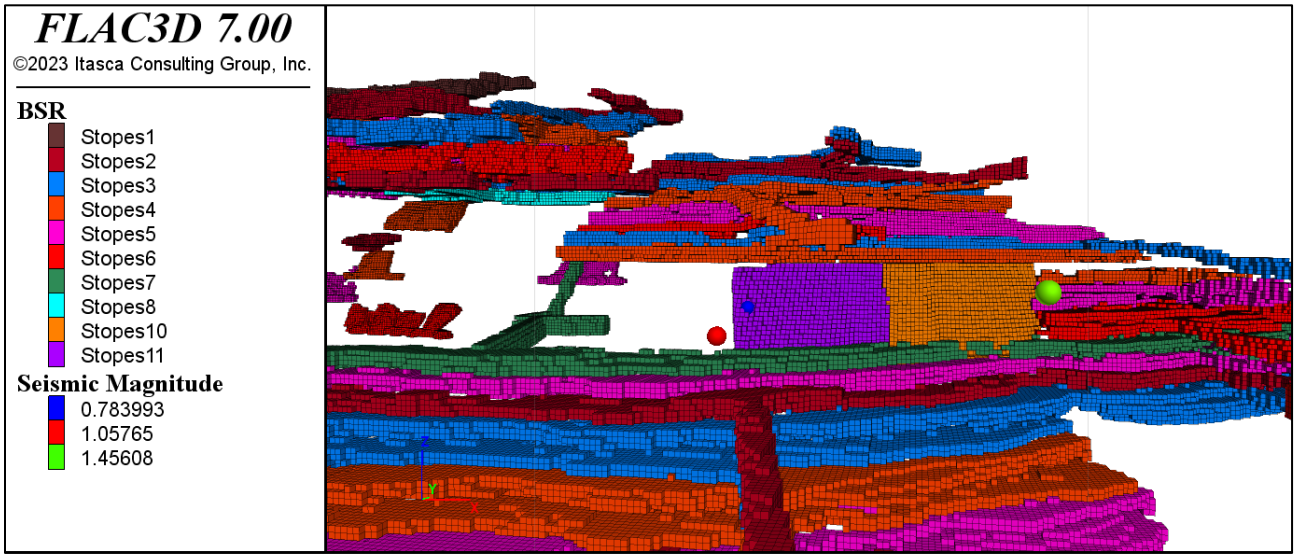

Figure 3.12: Front view of the stopes, spheres represent the seismic events while excavating the undercut with a magnitude over 0.5.

Based on the results from the numerical model, the empirical data base from the mine and the observations on the field, dynamic support was chosen according to the expected micro-seismicity. A representation of the dynamic support chosen is shown at Figure 3.13.

On the overcut, the support selected is the following:

- 20mm Versa bolts on 4ft x 4ft spacing, with dice bolts
- #6-gauge wire mesh screens
- #0-gauge straps on screen seams
- Support to sill/bench elevation.
- Arches at intersection about 70ft in all directions

On the undercut, the support selected is the following:

- 20mm Versa bolts on 4ft x 4ft spacing, with dice bolts
- #6-gauge wire mesh screens

- #0-gauge straps on screen seams
- One section primarily supported with MD bolts and re-supported with Versa bolts on the same pattern without dice bolts.

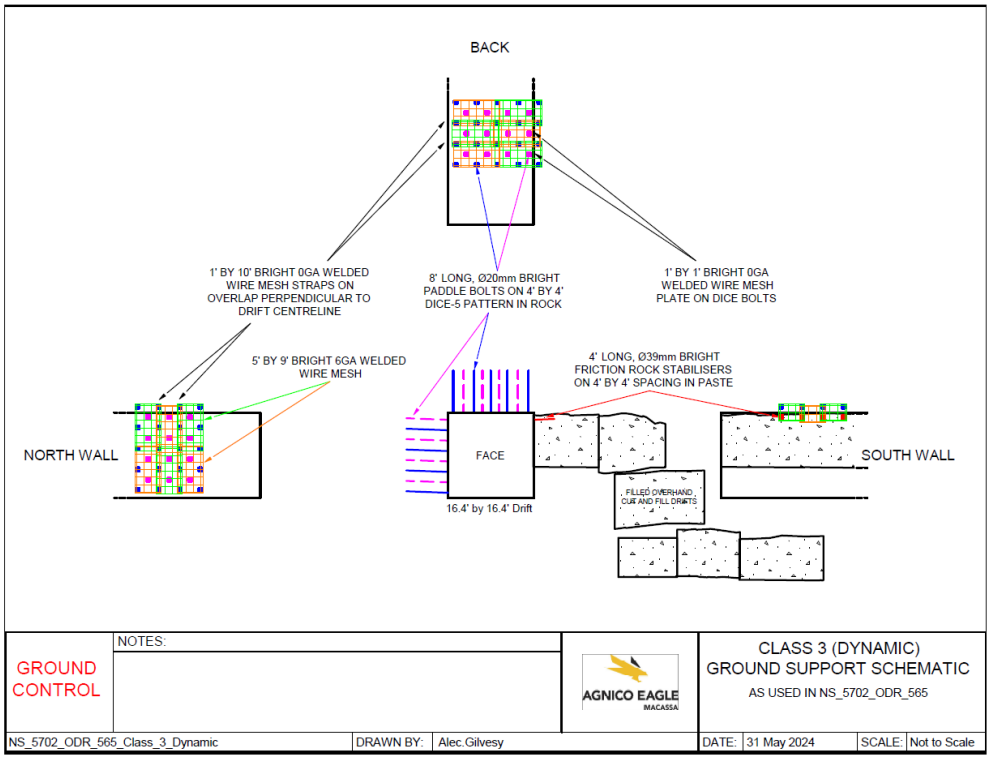

Figure 3.13: Dynamic support chosen for the undercut of the sill pillar.

3.6 Conclusion

Elastic 3D modelling results were able to demonstrate a stable ore pillar during pre-mining and post blast within the sill pillar. BSR plots indicate the core of the pillar during overcut and undercut development is below the 0.6 threshold for generating critical particle ejection velocities for this sill pillar case. Higher BSR and BPI values compared to the pillar core were modelled within 2m of the excavation surfaces but still plotted below the BSR 0.6 and BPI 0.2 thresholds. These results agree with field observations and seismic response from sill development and long hole drilling activities and, therefore, the use of BSR and BPI indexes are great indicators for seismic hazard. Derived kinetic energy and dynamic support capacity calculations indicate the current support system in place is appropriate for mining induced seismicity under current rock mass conditions.

Future modelling work is required to adequately consider the effect of significant rock mass deformation on stress redistribution to the remaining sill pillar once the first stope is blasted. The

resultant BSR and BPI index thresholds, and derived kinetic energy calculations, can then be further refined for pillar stability and ground support capacity evaluations. Post blast reconciliation with future modelling works will be an imperative effort required to evaluate tactical controls in managing seismic risk as sill pillar mining progresses.

These modelling derivations can be used to evaluate dynamic capacities of ground support systems, with the goal to achieve a desired Factor of Safety for expected seismic levels. Support dynamic capacity calculations rely on critical case for kinetic energy per unit of area. This case assumes a higher velocity than the ones found on previous events. Further research on the establishment of the BSR threshold is needed as it is another important aspect of the kinetic energy calculation.

Acknowledgement

We would like to express our sincere gratitude to the Natural Sciences and Engineering Research Council of Canada – NSERC Discovery Program, Grant RGPIN/05645-2020, for their financial support. Additionally, we extend our appreciation to Agnico Eagle Mines Limited for providing valuable information and insights that greatly contributed to the success of this study.

References

Blake, W. 1972, 'Rock-burst mechanics', *Quarterly of the Colorado School of Mines*, vol. 67, no. 1, pp. 1–64.

Blake, W. & Hedley, D. 2003, 'Rockbursts, Case Studies from North American Hard-rock Mines', *Society for Mining, Metallurgy and Exploration,* New York.

Butcher, R., Ball, R., Hartmann, B., Currie, J. & McLeay, G. 2005, 'Ground Support Optimisation at Long Shaft', in *Proceedings of the Sixth International Symposium on Rockburst and Seismicity in Mines Proceedings*, Australian Centre for Geomechanics, Perth, pp. 511-517.

Castro, L., Bewick, R. & Carter, T. 2012, 'An Overview of Numerical Modelling Applied to Deep Mining', *Innovative Numerical Modelling in Geomechanics*, pp. 393–414.

Gill, D., Aubertin, M. & Simon, R. 1993, 'A practical engineering approach to the evaluation of rockburst potential', in *Proceedings of the 3rd International Symposium on Rockbursts and Seismicity in Mines*, Proceedings of the 3rd International Symposium on Rockbursts and Seismicity in Mines, Rotterdam, Netherlands, pp. 63–68.

He, F. 2005, *Study on geological hazards in tunnelling of deep-buried long tunnels at Ginling-Dabashan orogen of the three gorges reservoir water diversion project*, PhD thesis, China Academy of Geological Sciences, Beijing.

He, M., Miao, J., Li, D. & Wang, C. 2007, 'Experimental study of rockburst processes of granite specimen at great depth', *Chinese Journal of Rock Mechanics and Engineering*, vol. 26, no. 5, pp. 865–876.

He, M., Xia, H., Jia, X., Gong, W., Zhao, F. & Liang, K. 2012, 'Studies on classification, criteria and control of rockbursts', *Journal of Rock Mechanics and Geotechnical Engineering*, vol. 4, no. 2, pp. 97–114.

Heal, D. 2010, *Observations and analysis of incidences of rockburst damage in underground mines*, PhD thesis, University of Western Australia.

Hedley, D. 1992, 'Rockburst Handbook for Ontario Hardrock Mines', *CANMET Special Report SP92-1E*, Communication Group, Ottawa, Canada.

Itasca Consulting Group, Inc. 2019, FLAC3D — Fast Lagrangian Analysis of Continua in Three-Dimensions, Version 7.0, Minneapolis: Itasca.

Kaiser, P., Tannant, D. & McCreath, D. 1996, 'Canadian Rockburst Support Handbook', *Geomechanics Research Centre*, Laurentian University, Sudbury, Ontario.

Kaiser, P. & Cai, M. 2018, 'Rockburst phenomena and support characteristics', *Rockburst Support Reference Book*, vol. I, Laurentian University.

Khalil, H. 2023, *Effect of mining and geology on induced seismicity – A case study*, Master's Thesis, McGill University, Montreal, Quebec, Canada.

Mitri, H., Tang, B. & Simon, R. 1999, 'FE modelling of mining-induced energy release and storage rates', *Journal of the South African Institute of Mining and Metallurgy*, vol. 99, no. 2, pp. 103–110.

Ortlepp, W. 1992, 'The design of support for the containment of rockburst damage in tunnels - an engineering approach', in *Proceedings of International Symposium on Rock Support in Mining and Underground Construction*, Laurentian University, Sudbury, pp. 593-609.

Ortlepp, W. & Stacey, T. 1994, ‘Rockburst mechanisms in tunnels and shafts’, *Tunnelling and Underground Space Technology*, vol. 9 no. 1, pp. 59–65.

Ortlepp, W. 1997, ‘Rock fracture and rockbursts: an illustrative study’, *South African Institute of Mining and Metallurgy*.

Solak, T. 2009, ‘Ground behavior evaluation for tunnels in blocky rock masses’, *Tunnelling and Underground Space Technology*, vol. 24, no. 3, pp. 323–330.

Bridging text between manuscripts

In the previous part of this thesis, reported in Chapter 3, the recovery of a deep sill pillar in Macassa mine was evaluated. The results from the numerical model were discussed and the importance of the mining sequence was highlighted as it could play an important role on the occurrence of rockburst events. Macassa Mine is a case with bursting material and the sill pillar is located in the deep part of the mine where the stresses are high and bursting is more likely to happen. On the other hand, Young-Davidson (YD) Mine, of Alamos Gold Inc. in northern Ontario, Canada, is a shallow depth mine which has been experiencing seismicity over the last few years. The following chapter reports on the testing procedures for the lithologies of YD Mine. The testing program is important for the characterization of the mechanical properties. Following the American Society for Testing and Materials Standards, it is necessary to comply with the suggested requirements for the testing of rock cores in Uniaxial Compressive Strength (UCS) and Brazilian Tensile Strength (BTS) tests. Sample preparation will determine the fitness of the samples to assess the validity of the tests. Chapter 4 is followed by Chapter 5 which will show the results of the testing program at YD Mine. These results will be used as inputs for the Mine-wide numerical model of YD Mine to evaluate the possible causes behind the seismicity in a shallow depth mine.

Chapter 4 - Experimental program for Young-Davidson Mine

4.1 Introduction

This chapter is about a testing program for Young-Davidson (YD) mine of Alamos Gold Inc. in northern Ontario, Canada. It is a gold mining operation which uses the sublevel stoping method. The mine can operate at 8,000 tonnes per day, and it is accessed via two shafts and a ramp system. The mineralization reaches depths of 1,500 m (Khalil et al., 2024). Recent research (Khalil, 2023, Khalil et al., 2024) attempted to explain the large seismic events by using different criteria on the seismic database to further understand the reasons behind large seismic events. One of the main limitations to further assess the stress state of the mine was the limited information on rock burstability. In this chapter, a test program is implemented to assess the properties of the materials as an initial step towards a better representation of the current stress state of the mine using numerical modelling tools with the update of the lithologies on the previous model of the mine (Khalil et al., 2024). A series of UCS, BTS and Load-Unload tests are carried out in order to determine the burstability of the rocks as well as the rock mass properties.

In this chapter, the experimental procedure of the different tests used for assessing the material properties of the lithologies of the second study case of this thesis, Young-Davidson Mine, is described. A total of 114 specimens were tested in the Rock Bolting laboratory of the Mine Design.

The main objective of the experimental program is to determine the mechanical properties and rock burstability. The testing program consists of Brazilian Tensile Strength Test (BTS), Uniaxial Compressive Strength Test (UCS), and Uniaxial Loading and Unloading Test (LUN). It is important to remark that Young-Davidson Mine is a highly seismically active mine with some recorded events with a magnitude of over +2.0 (Khalil, 2023).

4.2 Lithologies

This section describes the information available about the lithologies present at Young-Davidson Mine. There are 6 lithologies identified:

- Sediments, part of the host rock.
- Basalt, fine-grained igneous rock. Part of the host rock.
- Sheared Sediments, related to sediments as well in the host rock.
- Barite, usually it is associated with the diabase. Part of the dykes.

- Diabase, main material of the dykes. It gets significantly weaker when there is presence of barite on it.
- Syenite, this is the ore of the Young-Davidson mine. Most of the events at the mine were reported on the syenite.

Figure 4.1 shows rock samples that were prepared for the core rocks received from YD Mine. Basalt, Diabase and Sediments are NQ core size (47.6 mm in diameter) while Barite, Sediments Sheared and Syenite are a BQ core size (36.5 mm in diameter).

Figure 4.1: Rock types tested for the Young-Davidson Mine deposit.

Basalt was retrieved from the level 9590; there was presence of veins of calcite and quartz dipping at approximately 65°. The basalt samples were drilled in the hanging wall. Sediments were retrieved from the level 9200 of the mine. They are associated with quartz and pyrite. Sediments are also part of the host rock, most of the time located in the footwall. Diabase was retrieved from the deeper levels of the mine from level 8990 to 9025. There are two main textures, fine and coarse grains. The fine grains are found next to the diabase boundary with the Syenite in the deeper parts of the mine. It is also the main component of the dykes present throughout the mine. These dykes tend to be larger than 20 meters wide. Barite is mostly present in the dykes. It is associated with diabase, and it weakens the properties of the dyke. Barite is the main component of the shear zones. Syenite is the main component of the ore. It has some veins of quartz and calcite. There is also presence of magnetite on small quantities. Most of the recorded seismic events were located on the syenite. Sediments sheared is the intermediate lithology between the sediments host rock and the barite shear zone.

4.3 Tests Performed

4.3.1 Uniaxial Compressive Strength (UCS) test

The uniaxial compressive Strength (UCS) test is an important test for rock geomechanics in mining (Clout & Manuel, 2015). This test relies on a uniaxial load applied to rock cores of different lengths

and diameters. The main objective of this test is to measure the compressive strength of a rock sample when subjected to uniaxial stress.

Figure 4.2 shows the UCS servo-controlled press from Controls Inc. It has a capacity of 2,000 KN and can be used in servo load or displacement control mode.

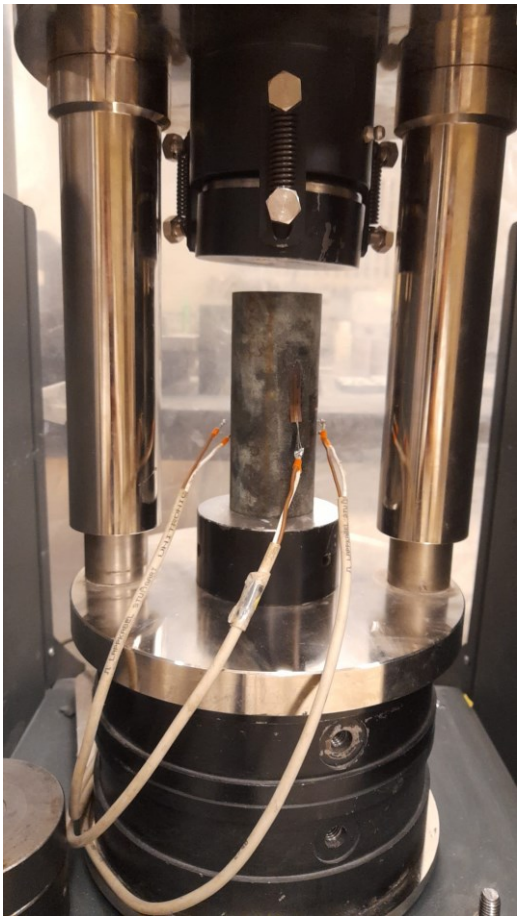

Figure 4.2: Servo-controlled UCS press.

The uniaxial compressive strength is defined as the ratio of the peak load to the cross-sectional area of the rock sample. It is given by

$$\sigma_C = \frac{P}{A} \tag{4.1}$$

where:

σ_c = Uniaxial compressive strength of the rock (in MPa)

P = Peak or failure load (in N)

A = Cross-sectional area (in mm^2)

The Young's modulus of elasticity is defined as the tangent modulus measured at 50% of the UCS as shown in Equation 4.2.

$$E_t = \frac{\Delta\sigma}{\Delta\varepsilon} \tag{4.2}$$

where:

E_t = Young Modulus (in GPa)

$\Delta\sigma$ = Increment of the stress at 50% UCS (in MPa)

$\Delta\varepsilon$ = Increment of the strain at 50% UCS

Finally, the Poisson's ratio is defined as the relation between the lateral strain divided by the vertical strain, usually measured at 50% UCS. Equation 4.3 shows the formula to determine the Poisson's ratio.

$$v = -\frac{\varepsilon_h}{\epsilon_v} \tag{4.3}$$

where:

v = Poisson's ratio

E_t = Young's modulus (in GPa)

4.3.2 Brazilian Tensile Strength (BTS) test

The Brazilian Tensile Strength (BTS) test is an indirect testing method to calculate the tensile strength on rock cores. According to the ASTM 3967 (2016), the ratio between the thickness to diameter of the sample should be at least 0.2 and can go up to 0.75. A lower ratio may cause the disk to behave like a thin plate and inaccurate stress distribution could occur, while a higher ratio could risk of shear failure instead of tensile splitting. It is estimated from Equation 4.4 as follows.

$$\sigma_t = \frac{2P}{\pi D t} \tag{4.4}$$

where:

σ_t = Tensile strength of the rock (in MPa)

P = Maximum applied load at failure of the rock sample (in N)

D = Diameter of the specimen (in mm)

t = Thickness of the specimen (in mm)

4.3.3 Uniaxial Load-Unload (LUN) test

The purpose of the LUN test is to measure the plastic energy dissipated in fracturing during loading and the elastic energy recovered during unloading. The process for this test is to load the sample to a percentage of its estimated UCS from previous tests then unload it. Upon unloading, a new loading cycle is started with a higher load value than the previous cycle. Based on previous results (Malki et al., 2024), in this thesis, the ranges of 70, 77 and 85% were selected as the 3 cycles proposed for each sample. The dissipated plastic energy from each cycle is added to the next cycle. This should lower the elastic strain energy storage index W_{et} , defined in Equation 2.1, after each cycle.

4.4 Sample preparation

Rock sample preparation was done in accordance with the American Society for Testing and Materials ASTM D4543-19 (American Society for Testing and Materials, 2019) for the UCS and LUN tests. The length-to-diameter aspect ratio is kept between 2 and 2.5 and samples were checked for shape tolerances, straightness, flatness, perpendicularity and parallelism prior to testing. Samples for the BTS tests complied with ASTM D3967-16 (American Society for Testing and Materials International, 2016) for the thickness-to-diameter ratio of 0.2 to 0.75. Figure 4.3 shows a flowchart used on the Rock bolting Laboratory as part of the shape conformance verification of cylindrical rock sample and Table 4.1 shows the sample information related to the UCS, LUN and BTS tests.

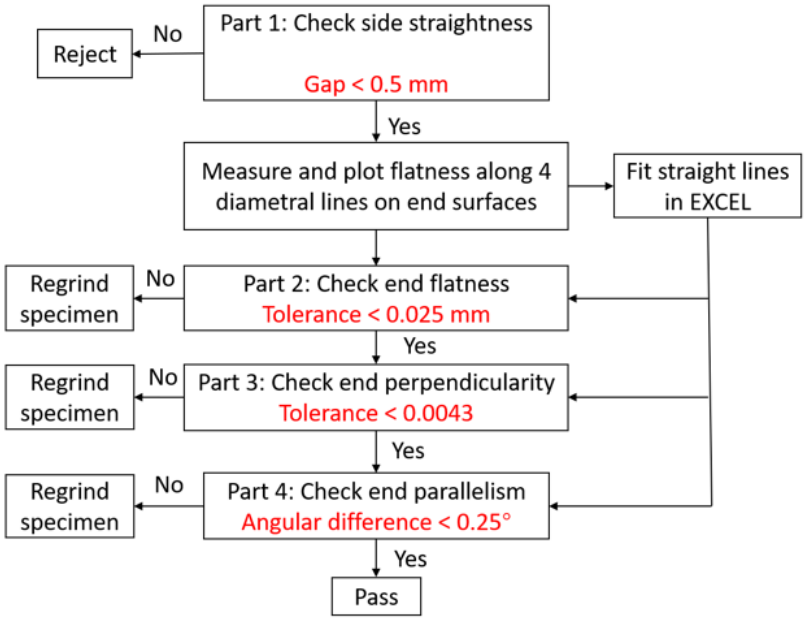

Figure 4.3: Flowchart for rock sample preparation.

Table 4.1: Samples tested for different rock types at Young-Davidson Mine.

Lithology	Sample ID	Test performed	D, L, L/D ratio or D, T, T/D ratio for BTS
Basalt	BAS-UC1	UCS	47.65 mm, 114.36 mm, 2.4
	BAS-UC2		47.65 mm, 113.01 mm, 2.4
	BAS-UC3		47.65 mm, 115.27 mm, 2.4
	BAS-LUN1	LUN	47.65 mm, 114.98 mm, 2.4
	BAS-LUN2		47.65 mm, 115.02 mm, 2.4
	BAS-LUN3		47.65 mm, 114.83 mm, 2.4
	BAS-BT1	BTS	47.65 mm, 11.27 mm, 0.24
	BAS-BT2		47.65 mm, 11.33 mm, 0.24
	BAS-BT3		47.65 mm, 11.92 mm, 0.25
	BAS-BT4		47.65 mm, 11.24 mm, 0.24
	BAS-BT5		47.65 mm, 11.7 mm, 0.25

	BAS-BT6		47.65 mm, 11.21 mm, 0.24
	BAS-BT7		47.65 mm, 11.62 mm, 0.24
	BAS-BT8		47.65 mm, 11.38 mm, 0.24
	BAS-BT9		47.65 mm, 11.84 mm, 0.25
	BAS-BT10		47.65 mm, 11.72 mm, 0.25
Diabase	DIA-UC1	UCS	47.65 mm, 114.28 mm, 2.4
	DIA-UC2		47.65 mm, 114.46 mm, 2.4
	DIA-UC3		47.65 mm, 114.8 mm, 2.4
	DIA-LUN1	LUN	47.65 mm, 115.08 mm, 2.4
	DIA-LUN2		47.65 mm, 115.93 mm, 2.4
	DIA-LUN3		47.65 mm, 115.15 mm, 2.4
	DIA-BT1	BTS	47.65 mm, 11.86 mm, 0.25
	DIA-BT2		47.65 mm, 12.06 mm, 0.25
	DIA-BT3		47.65 mm, 12.08 mm, 0.25
	DIA-BT4		47.65 mm, 12.09 mm, 0.25
	DIA-BT5		47.65 mm, 12.75 mm, 0.27
	DIA-BT6		47.65 mm, 12.03 mm, 0.25
	DIA-BT7		47.65 mm, 12.06 mm, 0.25
	DIA-BT8		47.65 mm, 12.22 mm, 0.26
	DIA-BT9		47.65 mm, 11.98 mm, 0.25
	DIA-BT10		47.65 mm, 11.88 mm, 0.25
Sediments	SED-UC1	UCS	47.65 mm, 114.75 mm, 2.4
	SED-UC2		47.65 mm, 114.66 mm, 2.4

	SED-UC3		47.65 mm, 114.03 mm, 2.4
	SED-LUN1	LUN	47.65 mm, 115.42 mm, 2.4
	SED-LUN2		47.65 mm, 115.23 mm, 2.4
	SED-LUN3		47.65 mm, 115.86 mm, 2.4
	SED-BT1	BTS	47.65 mm, 12.60 mm, 0.26
	SED-BT2		47.65 mm, 12.45 mm, 0.26
	SED-BT3		47.65 mm, 12.55 mm, 0.26
	SED-BT4		47.65 mm, 12.37 mm, 0.26
	SED-BT5		47.65 mm, 12.66 mm, 0.27
	SED-BT6		47.65 mm, 12.55 mm, 0.26
	SED-BT7		47.65 mm, 12.52 mm, 0.26
	SED-BT8		47.65 mm, 12.46 mm, 0.26
	SED-BT9		47.65 mm, 12.52 mm, 0.26
	SED-BT10		47.65 mm, 12.65 mm, 0.27
Sediments sheared	SSE-UC1	UCS	36.13 mm, 77.51 mm, 2.2
	SSE-UC2		36.13 mm, 78.45 mm, 2.2
	SSE-UC3		36.13 mm, 78.97 mm, 2.2
	SSE-LUN1	LUN	36.13 mm, 79.51 mm, 2.2
	SSE-LUN2		36.13 mm, 78.11 mm, 2.2
	SSE-LUN3		36.13 mm, 77.55 mm, 2.2
	SSE-LUN4		36.13 mm, 79.13 mm, 2.2
	SSE-LUN5		36.13 mm, 78.02 mm, 2.2
	SSE-LUN6		36.13 mm, 78.11 mm, 2.2

	SSE-BT1	BTS	36.13 mm, 9.27 mm, 0.26
	SSE-BT2		36.13 mm, 9.35 mm, 0.26
	SSE-BT3		36.13 mm 9.47 mm, 0.26
	SSE-BT4		36.13 mm, 9.34 mm, 0.26
	SSE-BT5		36.13 mm, 9.54 mm, 0.26
	SSE-BT6		36.13 mm, 9.38 mm, 0.26
	SSE-BT7		36.13 mm, 9.35 mm, 0.26
	SSE-BT8		36.13 mm, 9.57 mm, 0.26
	SSE-BT9		36.13 mm, 9.39 mm, 0.26
	SSE-BT10		36.13 mm, 9.47 mm, 0.26
Syenite	SYE-UC1	UCS	36.13 mm, 79.59 mm, 2.2
	SYE-UC2		36.13 mm, 78.53 mm, 2.2
	SYE-UC3		36.13 mm, 79.15 mm, 2.2
	SYE-LUN1	LUN	36.13 mm, 79.14 mm, 2.2
	SYE-LUN2		36.13 mm, 78.83 mm, 2.2
	SYE-LUN3		36.13 mm, 78.63 mm, 2.2
	SYE-LUN4		36.13 mm, 79.5 mm, 2.2
	SYE-LUN5		36.13 mm, 77.48 mm, 2.2
	SYE-LUN6		36.13 mm, 77.91 mm, 2.2
	SYE-BT1	BTS	36.13 mm, 10.02 mm, 0.28
	SYE-BT2		36.13 mm, 10.17 mm, 0.28
	SYE-BT3		36.13 mm, 10.08 mm, 0.28
	SYE-BT4		36.13 mm, 9.81 mm, 0.27

	SYE-BT5		36.13 mm, 10.05 mm, 0.28
	SYE-BT6		36.13 mm, 10.21 mm, 0.28
	SYE-BT7		36.13 mm, 10.03 mm, 0.28
	SYE-BT8		36.13 mm, 10.07 mm, 0.28
	SYE-BT9		36.13 mm, 10.22 mm, 0.28
	SYE-BT10		36.13 mm, 10.06 mm, 0.28
Barite	BAR-UC1	UCS	36.13 mm, 77.61 mm, 2.2
	BAR-UC2		36.13 mm, 77.8 mm, 2.2
	BAR-UC3		36.13 mm, 79.04 mm, 2.2
	BAR-LUN1	LUN	36.13 mm, 79.15 mm, 2.2
	BAR-LUN2		36.13 mm, 79.5 mm, 2.2
	BAR-LUN3		36.13 mm, 78.6 mm, 2.2
	BAR-LUN4		36.13 mm, 78.6 mm, 2.2
	BAR-LUN5		36.13 mm, 79.57 mm, 2.2
	BAR-LUN6		36.13 mm, 79.78 mm, 2.2
	BAR-BT1	BTS	36.13 mm, 7.83 mm, 0.22
	BAR-BT2		36.13 mm, 8.07 mm, 0.22
	BAR-BT3		36.13 mm, 8.28 mm, 0.23
	BAR-BT4		36.13 mm, 8.24 mm, 0.23
	BAR-BT5		36.13 mm, 8.33 mm, 0.23
	BAR-BT6		36.13 mm, 8.33 mm, 0.23
	BAR-BT7		36.13 mm, 8.37 mm, 0.23
	BAR-BT8		36.13 mm, 8.31 mm, 0.23

	BAR-BT9		36.13 mm, 8.30 mm, 0.23
	BAR-BT10		36.13 mm, 8.26 mm, 0.23
	BAR-BT11		36.13 mm, 13.17 mm, 0.37
	BAR-BT12		36.13 mm, 13.30 mm, 0.37
	BAR-BT13		36.13 mm, 13.84 mm, 0.39
	BAR-BT14		36.13 mm, 13.19 mm, 0.37

To comply with sample straightness, a feeler gauge, shown in Figure 4.4, is used. As the sample is rolled on a flat surface, the 0.5 mm feeler gauge is used to check the tolerance for straightness.

Figure 4.4: Feeler gauge used in the Rock bolting laboratory.

End flatness is checked by drawing two perpendicular diagonal lines the sampled end face. Once the centre is marked, ten equally spaced points are marked along each diagonal. With the core placed in the V-block apparatus as shown in Figure 4.5, a dial gauge is used to record out-of-plane topography (non-flatness) of the end. Once all the data is collected, best-fit lines are plotted from data on both ends.

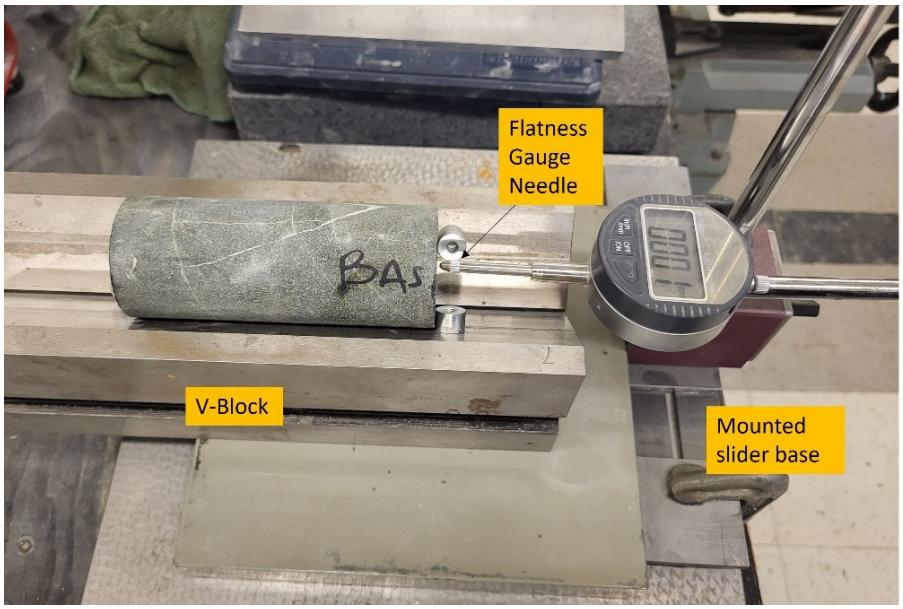

Figure 4.5: V-block apparatus used in the Rock bolting laboratory.

According to the ASTM-7012-04 (American Society for Testing and Materials, 2004), the flatness tolerance is met when the readings do not deviate from the best-fit straight line by more than 0.025 mm. Table 4.2 shows the results for the sample BAS-UC1. Figure 4.6 shows the resulting best-fit lines at End 1 and End 2.

Table 4.2: Example of the end surface flatness measurements.

Travel along diameter (mm)	Dial gauge measurement (mm)			
	End1, Dia1	End1, Dia2	End2, Dia1	End2, Dia2
0	0.01016	-0.01016	-0.00254	0.00254
5.2	0.00254	-0.00762	-0.00114	0
10.3	0	-0.00508	0.00029	0.00508
15.5	0.00254	-0.00508	0.00029	0
20.7	0	0	0	0
25.8	0	-0.00524	-0.01016	0.00345
31	-0.012	0.00492	-0.00762	0.00287
36.2	-0.0134	0.00746	-0.00762	0.00254
41.3	-0.0148	0.009	-0.00762	0.00123
46.5	-0.01524	0.01254	-0.00762	-0.00254

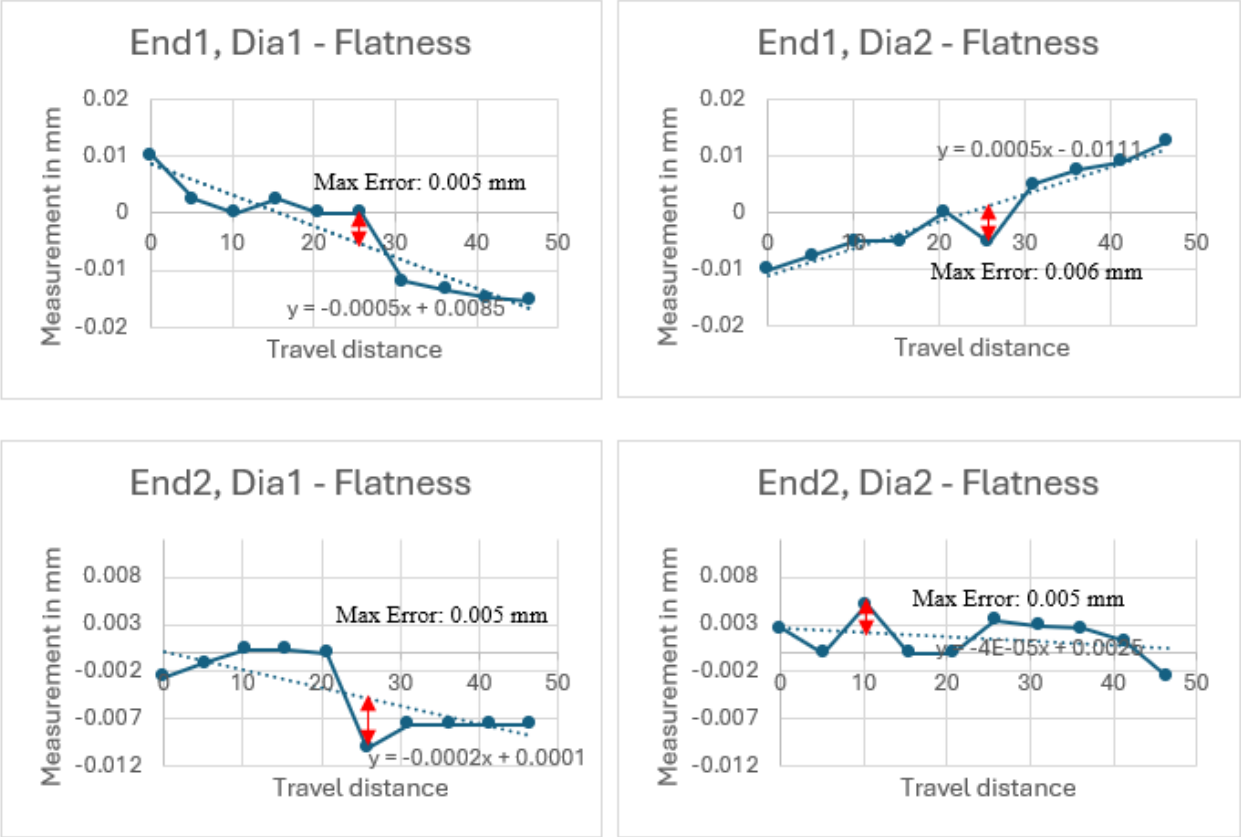

Figure 4.6: Results of the best-fit lines for BAS-UC1.

Next, end face perpendicularity is checked. Based on the information obtained to check the flatness of the end faces, it is possible to calculate the perpendicularity using the slope of the best-fit lines (diagonals).

Using the same example, Table 4.3 shows the results from the BAS-UC1 as an example. According to ASTM D-4543-19 (American Society for Testing and Materials, 2019) the perpendicularity is acceptable when the value of the slope of the best-fit line is below 0.0043.

Table 4.3: Perpendicularity of the faces' evaluation for BAS-UC1.

End Face – Diagonal Line	Slope of the best-fit line	Evaluation
End 1, Diagonal 1	-0.0005	Accepted
End 1, Diagonal 2	0.0005	Accepted
End 2, Diagonal 1	-0.0002	Accepted

End 2, Diagonal 2	-0.00004	Accepted

Finally, as the final parameter to be checked, parallelism of the end faces is also calculated from the information available on the excel spreadsheet. The angle of the best-fit line is calculated in degrees by using the tangent of the slope of each end face. If the difference between the end faces is less than 0.25° (American Society for Testing and Materials, 2019), then the parallelism is acceptable between the two faces. Table 4.4 shows the results for BAS-UC1 on parallelism.

Table 4.4: Parallelism of the end faces for the sample BAS-UC1.

End Face – Diagonal Line	Slope of the best-fit line	Angle inclination (°)	Difference	Evaluation
End 1, Diagonal 1	-0.0005	-0.02865		
End 1, Diagonal 2	0.0005	0.02865	0.0573	Accepted
End 2, Diagonal 1	-0.0002	-0.01146		
End 2, Diagonal 2	-0.00004	-0.00229	0.00917	Accepted

Following ASTM D4543 (2019), 3 strain gauges are placed, 2 verticals and 1 horizontal. The surface is cleaned with sanding paper of 320 and 400 grit size. A conditioner and spray activator are then applied to allow for better adhesion to the sample of the strain gauge. The specifications of the strain gauges used on the experiments are as follows.

- Resistance: 120 Ohm.
- Gauge factor: 2.11
- Transverse sensitivity: -0.3%
- Temperature compensation: 11 x 10E-6 /°C
- Length: 20 mm

The 3 gauges are placed at mid-height of the specimen and the vertical ones are on opposite sides of the specimen.

The only preparation needed for the BTS test is that the core is marked with a line parallel to the axis of the sample. This line is necessary to assure that the orientation of the applied loading on the sample is the same for all the experiments.

4.5 Test procedures

4.5.1 UCS test

For UCS, the parameters for the loading machine according to ASTM D7012-04 are:

- Loading rate between 0.5 to 1 MPa/s to ensure that the total test time is between 2 and 15 minutes.
- Peak sensitivity set at 50 KN.
- Peak load from 150 to 250 MPa, the test is concluded once sample failure occurs.

This configuration is done on the automatic system panel of the loading machine. The output of this experiment is to get the stress-strain curve of each sample until failure. The vertical values are averaged to get a better representation of the strain changes on the samples.

4.5.2 LUN Test

The parameters used for the LUN test are the same as those for UCS test. The main difference is that the LUN test is non-destructive as the applied load in each cycle is less than the UCS as previously explained.

4.5.3 BTS test

In the case of the BTS test, the parameters indicated in ASTM D7012-04 (American Society for Testing and Materials, 2004). The loading rate must be between 0.05 and 0.35 MPa/s and sample failure must occur between 1 and 10 minutes. The press is set to peak load sensitivity of 5 KN and the peak load limit is set to 50 KN.

In total, 109 rock samples were tested for the six lithologies presented in the Young-Davidson Mine.

References

American Society for Testing and Materials International. 2016. ASTM – D3967-16 Standard test method for splitting tensile strength of intact rock core specimens. Committee D18 on Soil and Rock, Subcommittee D18.12 on Rock Mechanics.

American Society for Testing and Materials International. 2016. ASTM – D3967-16 Standard test method for splitting tensile strength of intact rock core specimens. Committee D18 on Soil and Rock, Subcommittee D18.12 on Rock Mechanics.

American Society for Testing and Materials International. 2004. ASTM – D7012-04 Standard test method for Compressive Strength and Elastic moduli of intact rock core specimen under varying states of stress and temperatures. Committee D18 on Soil and Rock, Subcommittee D18.12 on Rock Mechanics.

Clout, J., Manuel, J. 2015. Mineralogical, chemical, and physical characteristics of iron ore. Iron Ore. Mineralogy, Processing and Environmental Sustainability, pp. 45-84.

Khalil, H., Chen, T., Blake, T., Thomas, A., Mitri, H. 2024. Analysis of induced seismicity at Young-Davidson mine. Deep Mining 2024. Australian Centre for Geomechanics, Perth.

Khalil, H. 2023. Effect of mining and geology on induced seismicity – A case study. Master's Thesis. McGill University, Montreal, Quebec, Canada.

Malki, J., Vennes, I., Rowe, C., Mitri, H. 2024. Evaluation of Rock Burstability with Mechanical Property testing and Microscopic Image Analysis. Rock Mechanics and Rock Engineering.

Bridging text between manuscripts

The following chapter reports on the case study of Young-Davidson (YD) Mine of Alamos Gold Inc. in northern Ontario, Canada. The evaluated case is of the cause of seismicity of the mine while it has relatively low depth. Nine events were reported with over 2.0 in Magnitude (Khalil et al., 2024). Mechanical rock properties were assessed following the test plan proposed in Chapter 4 of the present thesis. In total, 105 tests were performed on the lithologies present in YD mine. Based on the results, it was determined that the materials present in YD mine were not of burstable nature with low to moderate potential for violent and brittle failure. Among the factors that are possible to be controlled, the cause of seismicity for this case study which results in stress redistribution is likely to be due to two possible main reasons: geometric parameters of the sublevel stoping system which led to highly stressed secondary stopes and the high horizontal to vertical ratio which is located in an oblique angle of the mining direction at N45°E.

This paper is submitted to the Journal of Deep Resources Engineering.

Chapter 5 - Effect of mining geometry on mining induced burst events – A case study

5.1 Abstract

Rockburst is a complex problem which underground mines face around the world as they reach deposits at greater depths. It can be a serious threat to personnel safety and equipment damage, and as a result, could hinder productivity. Based on literature, it is well established that rockburst can be caused by numerous factors most notably geological features, mechanical rock properties, induced seismicity, and mining parameters. In this research, the Young Davidson (YD) Mine in Northern Ontario, Canada is used as the case study. The mine experiences seismic events at relatively shallow depths of less than 1 km. Previous studies at the mine have identified seismic source events in the ore pillars representing the secondary stopes. In the current study, rock burstability is examined through a comprehensive rock testing program of the different YD Mine lithologies. It is found rock burstability potential is low to moderate at best. A 3D mine-wide numerical model was then built and the updated mechanical rock properties as well as measured in-situ stress regime were used. The stress analysis revealed that high stress concentration occurs in the ore pillars. Seismic events were attributed primarily due to two factors. First, the nature of the sublevel stoping system leads to highly stressed secondary stopes. Secondly, the in-situ stress tensor has an oblique orientation to the orebody strike with an exceptionally high horizonal to vertical stress in-situ stress ratio. These findings support the hypothesis that mining geometry can be an independent cause for mining-induced seismicity regardless of rock properties.

Keywords: rockburst, seismicity, mining safety, numerical modelling, rock core testing

5.2 Introduction

Seismicity is observed in underground mines because of excavation activities (Gibowickz, 1990). It is a major safety concern for the mining industry and can pose significant challenges in deep producing mines (Gibowickz, 1990). Many factors can induce seismicity in mines such as depth, production rate, mining geometry and/or geological features (Mendecki, 1997, Holub, 1997, Guha, 2000). There are many cases of mining-induced seismicity that are reported from mines around the world such as South America and China (Dunlop and Gaete, 2001, Li et al., 2005) where strong seismic events were attributed to strong, brittle rocks and the presence of geological features such

as faults and dykes. However, in some cases, seismic events occurred in non-burstable rocks with no surrounding geological structures identified. In the following, a brief review will present some of such cases where major seismic events took place in the absence of strong rocks and geological structures.

The Australian mine “Strzelecki” is located at 25 km from Kalgoorlie in Western Australia. It has a narrow vein mineralization and a shear zone which is dipping steeply. There were some events with a magnitude greater than +1.5 ML, specifically near the center of the ore pillars due to stress concentration. An important consideration is the mining sequence with diminishing pillars, also a mining method of underhand long hole with benching starting at the extremities retreating towards the center. This area specifically is labeled as high risk (Heal, 2010).

The Australian mine Long Shaft, located in the Kambalda area, had always been labeled as one of the most challenging mines in Australia due to the geotechnical environment. It has a high horizontal stress field. While there were some events throughout the year, mainly strainburst at the developments, a concerning problem appeared when mining activities approached the crown pillar. Mechanized stoping and up-hole benching were used for ore extraction. These methods led to stress concentration in the diminishing pillar where no major geological structures were found. Also, some events occurred in low-strength ore rocks of 140 MPa of uniaxial compressive strength (Butcher et al., 2005).

The Quirke mine is in Elliot Lake in Ontario; it used to be a uranium mine and is currently undergoing environmental monitoring. It was commonly known for its pillar mining methods which led to many rockburst events. The orebody was a narrow sub-horizontal vein with massive quartzite in the footwall and hanging wall. According to Blake and Hedley (2009), the main problem associated with rockbursts was the orientation of the pillars of 45° with respect to the mining front. Events of over 2 in magnitude for some cases were recorded while no major geologic features were identified. Violent pillar failure was attributed to the design of the rib pillars at least in the upper part of the mine (Blake and Hedley, 2009).

Macassa Mine, in northern Ontario, Canada, experienced seismicity which was suspected to be tightly related to production using shrinkage methods before the change was made to overhand cut and fill and long-hole mining. It was observed that seismicity increased as the sill pillars were

approached (Blake and Hedley, 2009). As a result, it was proposed to modify the mining method and the geometry to decrease the occurrence of stress concentrations and carry out destress blasting.

At Teck-Hughes mine in Ontario, Canada, small magnitude strainbursts were reported as the mining sequence reached the sill pillars causing stress concentration around thin sill pillars at the top of the shrinkage stopes. In a similar way, Wright-Hargreaves mine in Ontario faced an increase of rockburst events towards the end of the mine life associated with the extraction of remnant pillars. The rate of major events annually increased to three times in the last year of the mining operation with events having a magnitude of over 3.1 (Blake and Hedley, 2009).

Another case in Ontario is at the Copper Cliff North Mine in Sudbury where many large rockburst events occurred in 1987 and 1988. Most events were in the pillars, and no geological structures were blamed for the seismic activity. The proposed solution was to alter the mining system to a center-out sequence instead of a primary-secondary approach. The result was an important decrease in the magnitude and frequency of the events (Morrison and Galbraith, 1990).

The Campbell mine, in Red Lake in Ontario, is well known for its rockburst events, which are almost exclusively related to sill pillar mining. Most rockbursts induced were the result of the redirection of the stress path due to changes in mine geometry. Increased production rates and large-size blasts were also identified as contributing factors (Hedley, 1992).

Lucky Friday mine in Idaho is another example of how mining geometry plays a dominating role in rockburst occurrence. The mine initially used overhand cut-and-fill as the main mining method. Rockburst events became a serious issue to deal with, and for that reason the implementation of a center-out stope mining geometry was necessary. The solution was based on reducing the stope strike length to allow for the transfer of stresses gradually.

Considering the above, the consensus is that strong seismicity can be attributed to mine geometry, with the addition of other factors like increased mining rates and production blast size. That said, none of the abovementioned studies reported a detailed geotechnical investigation into the rock mechanical properties to reveal the true causes for bursting activities. In the current study, rock burstability is first examined through a comprehensive rock testing program of the different YD Mine lithologies to establish their proneness to bursting. This will be followed by a stress analysis

of the YD mining system using 3D mine-wide modelling to help assess the influence of the mining geometry on mining-induced seismicity.

5.3 Case Study

The YD Mine is a gold mining operation which uses sublevel stoping method to reach their target production of 8,000 tonnes per day. The mine has been experiencing seismic events of over Mn 2.0 at relatively shallow depths (Khalil et al., 2024). Table 5.1 lists the major events recorded in 2021. For the geotechnical investigation, six lithologies were identified namely 1) sediments and 2) basalt, which are the main component of the host rock, 3) diabase and 4) barite, which are the main component of the dykes, 5) syenite, main component of the ore, and 6) sheared sediments, found in some parts within the host rock, associated with a transition part of the sediments. Most of the seismic events were reported in the syenite. Figure 5.1 shows photographs of typical rock samples prepared for testing.

Table 5.1: Parameters of the seismic events recorded in Young-Davidson Mine (Khalil et al., 2024).

Event Number	Moment Magnitude	Coordinates (x, y, z*)	Date
1	2.02	(23250, 10354, 9413)	02-06-2022
2	2.36	(23252, 10314, 9434)	05-06-2021
3	2.3	(23234, 10322, 9396)	05-17-2021
4	2.27	(23193, 10267, 9381)	06-30-2021
5	2.28	(23247, 10365, 9407)	07-18-2021
6	2.03	(23250, 10373, 9357)	08-26-2021
7	2.07	(23246, 10282, 9249)	09-04-2021
8	2.39	(23294, 10346, 9393)	10-16-2021
9	2.02	(23218, 10349, 9288)	02-10-2022

*Measured from ground surface elevation of 10,300 m.

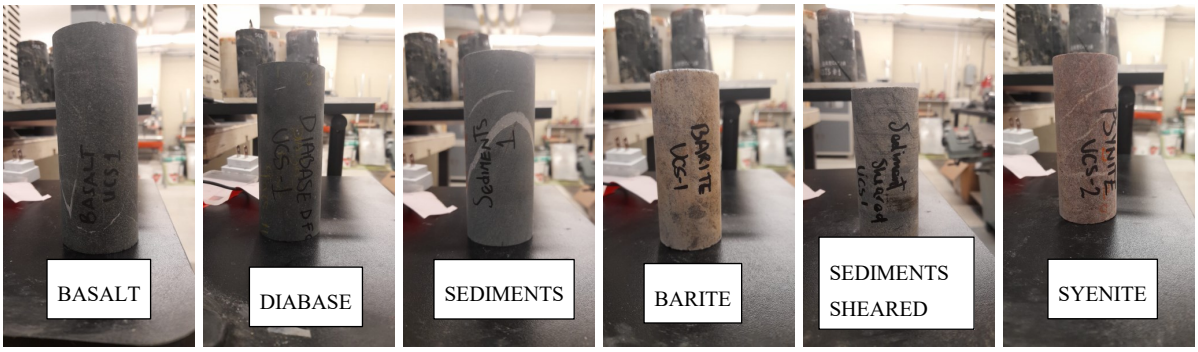

Figure 5.1: Lithologies present in Young-Davidson Mine for testing.

5.4 Rock burstability Assessment

5.4.1. UCS Tests

To assess the variability on the properties of different rock cores, 3 uniaxial compressive strength (UCS) tests were conducted for each lithology. As each sample was instrumented with vertical and horizontal strain gauges, it was possible to determine the Young's modulus of elasticity, E, and the Poisson's ratio, ν. Table 5.2 summarizes the test results. The third sample in the basalt test series, BAS-UC3, is considered an outlier since it didn't reach 100 MPa. The sample failed prematurely along a vein making 65° with the horizontal. A similar situation occurred with the diabase sample DIA-UC2 where a vein close to 70° to the horizontal was identified as the cause for early failure. Of the tested series, basalt exhibited the highest average UCS of 169 MPa and sheared sedimented exhibited the stiffest response with an average E of 92 GPa. Figure 5.2 shows the UCS test of the core BAS-UC1.

Table 5.2: UCS test results.

Lithology	Sample ID	UCS (MPa)	E (GPa)	ν
Basalt	BAS-UC1	189.8	110	0.38
	BAS-UC2	148.1	68.4	0.26
	BAS-UC3	70*	80.7	0.34
	Average	169	89.2	0.32
Barite	BAR-UC1	120	58	0.45
	BAR-UC2	132	46	0.24

	BAR-UC3	142.6	55	0.26
	Average	131.5	53	0.32
Sheared Sediments	SSE-UC1	155.9	88.7	0.08
	SSE-UC2	120.8	93.9	0.28
	SSE-UC3	181.9	92.7	0.22
	Average	152.9	92	0.2
Sediments	SED-UC1	91.8	74.7	0.21
	SED-UC2	96.8	58.2	0.09
	SED-UC3	102.2	62	0.29
	Average	96.9	65	0.2
Diabase	DIA-UC1	123.2	81	0.03
	DIA-UC2	84.8*	65.4	0.18
	DIA-UC3	147.5	52.7	0.4
	Average	118.5	66.4	0.2
Syenite	SYE-UC1	186.3	85.7	0.26
	SYE-UC2	98.4	51.2	0.26
	SYE-UC3	118	70	0.14
	Average	134.2	69	0.2

*Note: these values are considered as outlier, the values will not be taken into account for the final average.

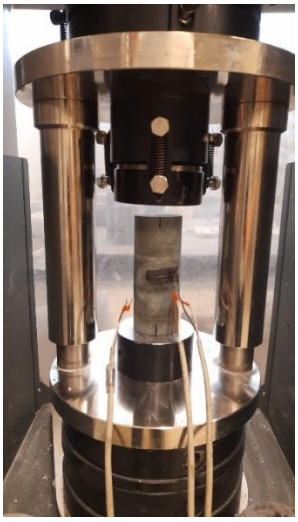

Figure 5.2: UCS test arrangement for sample BAS-UC1.

5.4.2 BTS Tests

The tensile strength of the rock is often used as a measure of the rock brittleness. According to Peng et al. (1996) and Zhang et al. (2012), the britttleness index (B) is defined by the ratio of the uniaxial compressive strength, UCS, to the tensile strength. Peng et al. (1996) proposed that when B < 14.5, the rock is considered highly brittle. In this study, the tensile strenght was determined using the Brazilian Tensile Strength (BTS) test. Thus, B=UCS/BTS.

Ten BTS tests were performed for each rock type following the recommendations of the American Society for Testing and Materials International (2016). It was determined that four additional tests of barite were needed as the samples BAR-BT7 to BT10 were visibly different from the others with a composition similar to sediments. Figure 5.3 shows the barite BTS tested samples.

Table 5.3 shows the BTS test results and calculated brittleness for each rock type. As can be seen, the sediments and shear sediments exhibited the largest BTS of 23.5 MPa 19.3 MPa and the lowest B values of 4.1 and 7.9, respectively, suggesting that such lithologies are brittle. On the other hand, the syenite rock exhibited less brittleness with an average B value of 14.7. It is noteworthy that syenite is the main component of the ore at the YD Mine, and this is where most seismic events were recorded.

Figure 5.3: Barite BTS tested samples. Note: samples BT7 to BT10 show a different mineral composition.

Table 5.3: BTS test and brittleness results.

Lithology	Specimen ID	BTS (MPa)	B
Basalt	BAS-BT1	12.9	
	BAS-BT2	13.9	
	BAS-BT3	12.6	
	BAS-BT4	9.6	
	BAS-BT5	9.2	
	BAS-BT6	13.6	
	BAS-BT7	12.5	
	BAS-BT8	13.8	
	BAS-BT9	14.4	
	BAS-BT10	11.9	
	Average	12.4	13.6

Lithology	Specimen ID	BTS (MPa)	B
Sediments Sheared	SSE-BT1	16.9	
	SSE-BT2	18.7	
	SSE-BT3	20.6	
	SSE-BT4	18.1	
	SSE-BT5	21.8	
	SSE-BT6	20.3	
	SSE-BT7	21.1	
	SSE-BT8	21.0	
	SSE-BT9	17.4	
	SSE-BT10	17.5	
	Average	19.3	7.9

Diabase	DIA-BT1	11.2	
	DIA-BT2	16.0	
	DIA-BT3	9.5	
	DIA-BT4	12.1	
	DIA-BT5	14.8	
	DIA-BT6	12.9	
	DIA-BT7	13.3	
	DIA-BT8	16.1	
	DIA-BT9	18.8	
	DIA-BT10	13.9	
	Average	13.9	8.5
Sediments	SED-BT1	24.3	
	SED-BT2	20.4	
	SED-BT3	21.6	
	SED-BT4	28.9	
	SED-BT5	26.8	
	SED-BT6	21.4	
	SED-BT7	26.1	
	SED-BT8	28.0	
	SED-BT9	18.4	
	SED-BT10	19.0	
	Average	23.5	4.1

Syenite	SYE-BT1	9.7	
	SYE-BT2	13.1	
	SYE-BT3	10.8	
	SYE-BT4	9.2	
	SYE-BT5	17.6	
	SYE-BT6	16.1	
	SYE-BT7	15.7	
	SYE-BT8	9.7	
	SYE-BT9	9.3	
	SYE-BT10	9.1	
	Average	12.0	14.7
Barite	BAR-BT1	7.7	
	BAR-BT2	8.1	
	BAR-BT3	7.1	
	BAR-BT4	6.0	
	BAR-BT5	8.1	
	BAR-BT6	7.7	
	BAR-BT11	3.4	
	BAR-BT12	7.4	
	BAR-BT13	6.9	
	BAR-BT14	6.5	
	Average	6.9	19.1

5.4.3 Load-Unload (LUN) tests

Based on experience from previous research, 3 loading cycles at 70%, 77% and 85% of the UCS value were used to assure that the core samples will not break (Malki et al., 2024). In some cases, due to the presence of geological structures or difference in mineral composition of the sample, the experiment can be stopped because the sample fails prematurely. It is important to note that the target UCS are based on the average from the test results shown in Table 5.2. Neyman et al. (1972) proposed the index W_{et} as the relation between the recovered elastic energy and the plastic energy in a load-unload (LUN), uniaxial compressive test as follows.

$$W_{et} = \frac{W_r}{W_p} \tag{5.1}$$

Based on this defintion, Kidybinski (1981) proposed ranges for bursting based on his observations. Table 5.4 shows the classification by Kidybinski (1981) to assess the bursting level based on the W_{et} index. Figure 5.4 depicts the different energy components of a LUN test.

Table 5.4: Classification of the W_{et} index for coal (Kidybinski, 1981).

W_{et}	Burst potential	Commentary
≥ 5	High	Fails in violent and dynamic mode with a broad spread of chips
5 > W_{et} > 2	Moderate	Intermediate failure behaviour
< 2	None	Quiet brittle fragmentation

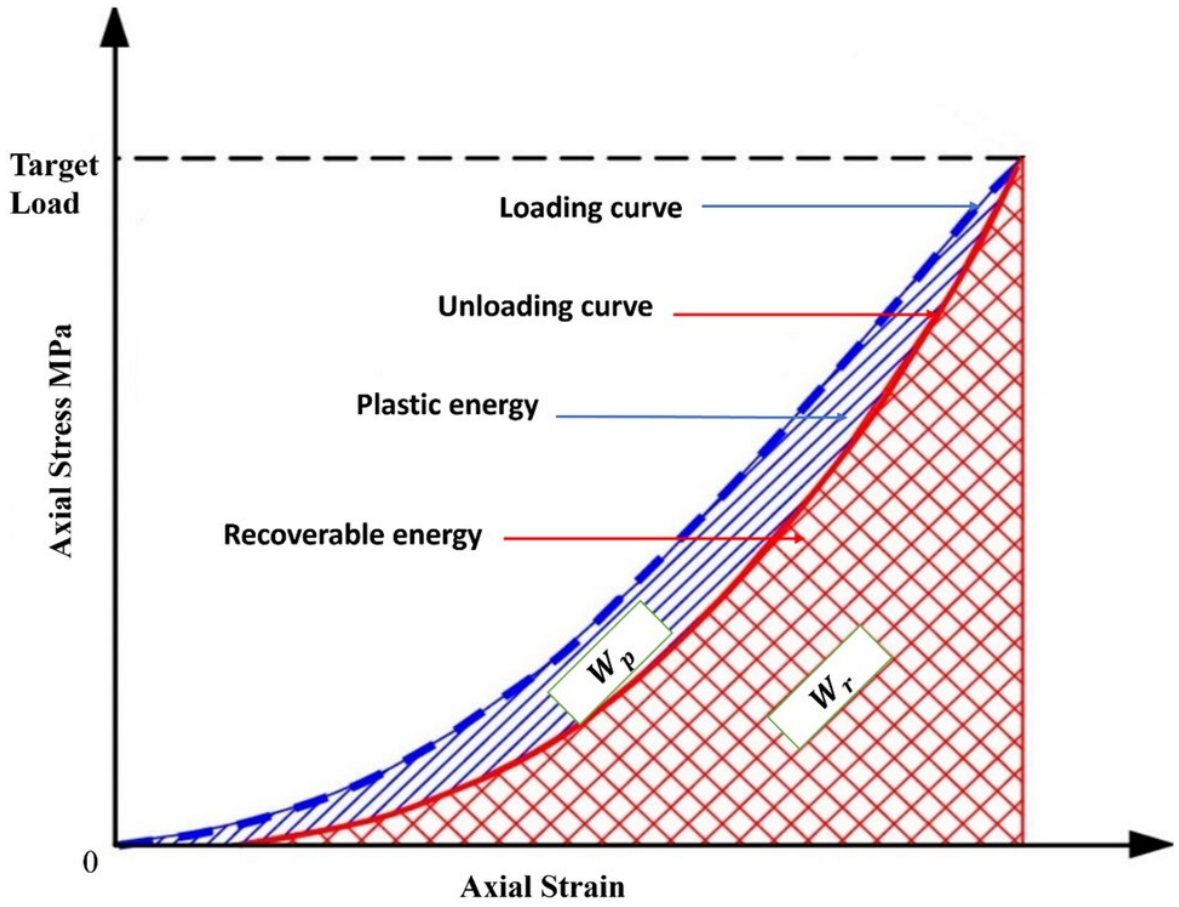

Figure 5.4: Energy components in a LUN test (Malki et al., 2024).

Table 5.5 lists the results of the LUN tests. Six tests were carried out for each of syenite and sheared sediments, three for each of sediments, diabase and basalt, and two for barite. Recoverable and plastic energy components are the most relevant outputs from a LUN test to assess rock burstability. Figure 5.5 displays a typical 3-cycle LUN test result for the sample BAS-LUN2.

Table 5.5: Results from the LUN tests.

Lithology	Sample	Cycle	Target Stress (MPa)	Wr (KJ/m^3)	Wp (KJ/m^3)
Basalt	BAS-LUN1	1	118.3	62.0	18.9
		2	130.1	84.8	29.0
		3	143.6	90.3	35.7
	BAS-LUN2	1	118.3	82.7	12.4
		2	130.1	94.3	20.9

		3	143.6	95.9	30.5
	BAS-LUN3	1	118.3	102.5	13.4
		2	130.1	104.7	21.2
		3	143.6	108.9	28.2
Diabase	DIA-LUN1	1	83.0	48.9	9.15
		2	91.2	65.4	15.3
		3	100.7	Broke at 79% of UCS	
	DIA-LUN2	1	83.0	Broke at 58% of UCS	
	DIA-LUN3	1	83.0	54.1	5.8
		2	91.2	71.7	10.6
		3	100.7	84.7	22.7
Sediments	SED-LUN1	1	67.9	39.2	6.2
		2	74.6	43.9	13.5
		3	82.4	44.1	31.3
	SED-LUN2	1	67.9	33.3	5.7
		2	74.6	37.9	12.2
		3	82.4	39.1	31.3
	SED-LUN3	1	67.9	38.3	5.6
		2	74.6	47.7	12.2
		3	82.4	54.1	32.2
Sheared Sediments	SSE-LUN1	1	107.0	59.6	9.13
		2	117.7	67.2	13.5
		3	129.9	73.3	25.8
	SSE-LUN2	1	107.0	57.7	9.64
		2	117.7	61.5	13.8

		3	129.9	67.0	29.4
	SSE-LUN3	1	107.0	60.3	6.74
		2	117.7	65.2	10.4
		3	129.9	74.2	23.2
	SSE-LUN4	1	107.0	37.7	5.7
		2	117.7	54.3	10.3
		3	129.9	59.9	30.9
	SSE-LUN5	1	107.0	36.3	6.5
		2	117.7	44.2	9.2
		3	129.9	37.6	12.3
	SSE-LUN6	1	107.0	89.2	15.4
		2	117.7	86.3	17.2
		3	129.9	97.6	28.2
Syenite	SYE-LUN1	1	94.0	59.5	8.2
		2	103.4	68.5	15.7
		3	114.1	72.9	27.2
	SYE-LUN2	1	94.0	64.3	7.6
		2	103.4	69.0	12.3
		3	114.1	72.3	21.2
	SYE-LUN3	1	94.0	50.5	7.1
		2	103.4	61.3	13.1
		3	114.1	66.6	23.8
	SYE-LUN4	1	94.0	58.7	7.5
		2	103.4	Broke at 72% of UCS	
	SYE-LUN5	1	94.0	Broke at 67% of UCS	

	SYE-LUN6	1	94.0	Broke at 65% of UCS	
Barite	BAR-LUN1	1	92.1	66.2	7.4
		2	101.3	71.8	13.5
		3	111.8	80.0	23.2
	BAR-LUN2	1	92.1	62.0	18.87

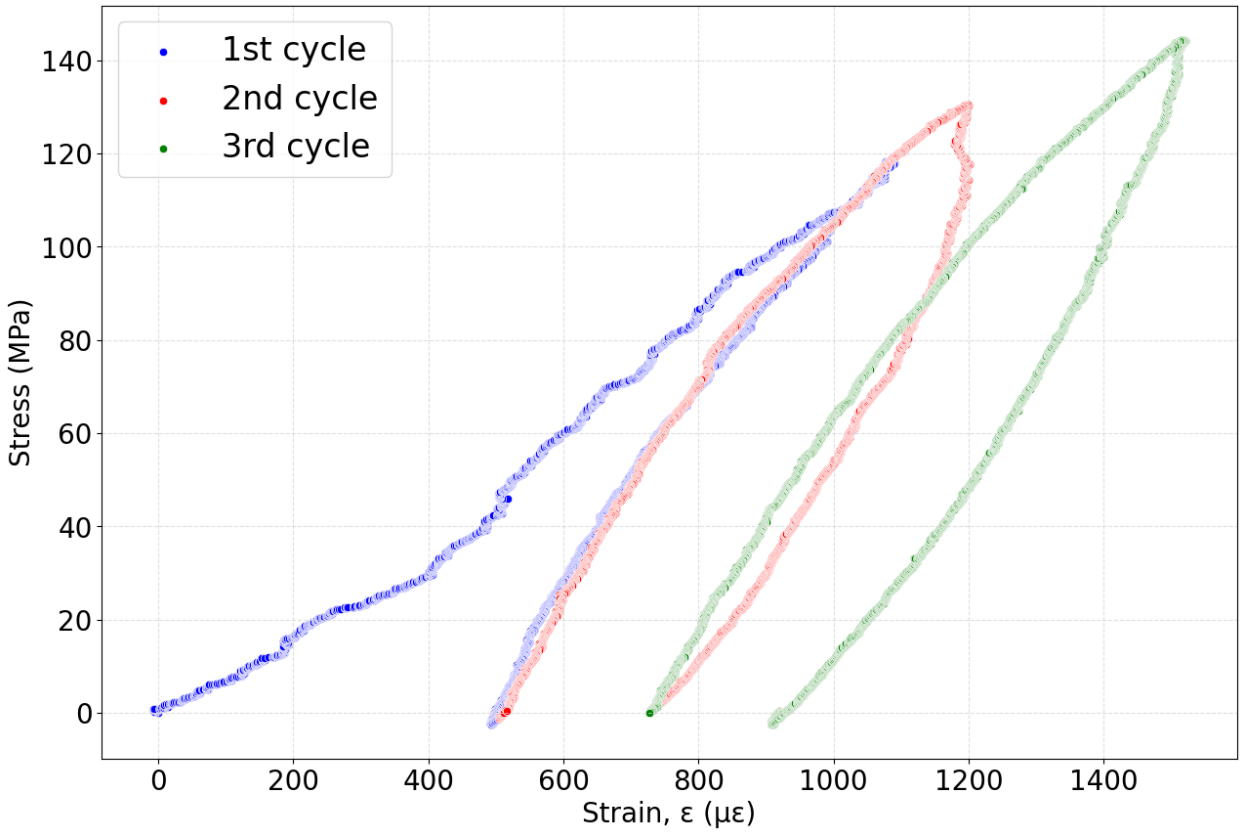

Figure 5.5: Typical Stress-strain curves, BAS-LUN2.

An additional tool to assess rock burstability was proposed by Wang and Park (2001) using the elastic strain energy density, SED, in a uniaxial compressive strength test as follows.

$$SED = \frac{UCS^2}{2\,E_s} \tag{5.2}$$

In the above, E_s is the modulus of elasticity. Wang and Park (2001) proposed SED values with specific ranges to describe the rockburst potential due to material properties. For $SED < 50$, the

rock is considered of very low rockburst hazard. A range of $50 < SED < 100$ reflects low rockburst hazard, and for $100 < SED < 150$, it reflects moderate rockburst hazard. Finally, for $150 < SED < 200$ high rockburst hazard is expected, and for $SED > 200$, very high rockburst hazard is anticipated. More recently, Cai (2016) suggested similar values albeit with SED < 40 for very low rockburst hazard, however, with SED > 200 for very strong rockburst hazard as proposed by Wang and Park (2001). As both studies recommended that an SED > 200 is indicative of a very high rockburst hazard, the same condition was adopted for the current study to indicate to highly-burstable rock. On the other hand, if SED < 100, it would represent low burstability. Table 5.6 shows the results of the rockburst assessment study for each lithology in terms of W_{et} and SED. As can be seen, none of the LUN tests showed a value of $W_{et} > 5$, and none of the ESR results exceeded 200. These results suggest that mining-induced seismic activity at YD Mine is not attributable to geotechnical properties of the lithologies. These findings are in line with the observations by Kaiser and Cai (2018) that mechanical rock properties, while important for understanding the mechanical behavior of the rock mass, are not always the primary cause for strong seismicity.

Table 5.6: Rock burstability assessment with SED and W_{et} (Kidybinski, 1981).

Lithologies	SED (KJ/m^3)	Rockburst hazard	W_{et} (LUN)	Burst potential
Basalt	107.1 < 200	Moderate	3.2 < 5	Moderate
Diabase	105.8< 200	Moderate	3.7 < 5	Moderate
Syenite	130.6< 200	Moderate	3 < 5	Moderate
Sheared Sediments	127.3< 200	Moderate	2.8 < 5	Moderate
Sediments	72.3< 100	Low	1.5 < 5	None
Barite	163.2< 200	Moderate	3.5 < 5	Moderate

5.5 Numerical model

The basic numerical model previously developed for YD Mine was developed by Khalil et al. (2024). The model was built with finite difference code FLAC3D (Itasca Ltd, 2019). In the absence of a detailed geotechnical database, the model treated the host rock and the orebody as one material representing all lithologies. In this study, the numerical model is updated with the new geotechnical properties obtained from the laboratory investigation presented earlier in this paper. The objective is to conduct a stress analysis to help interpret the cause for induced seismicity. The YD Mine has experienced numerous seismic events larger than Mn +1.5 in the last 4 years (Khalil et al., 2024). Figure 5.6 shows seismic source locations on a longitudinal view of the mine between levels 9830 and 9305, which correspond to mining depths of 470 m and 995 m, respectively. The figure shows seismic events of > 1.5 in Moment Magnitude between 2021 to 2022. As can be seen, most of the events are clustered around the production zone.

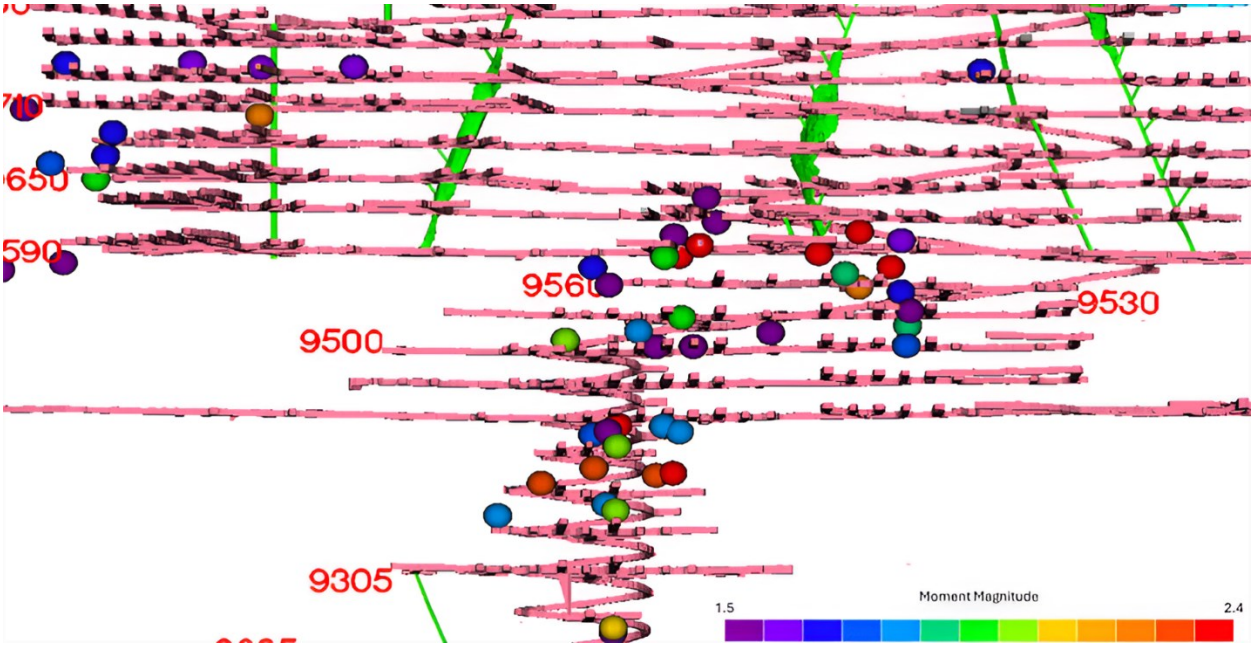

Figure 5.6: Seismic events above 1.5 in Moment Magnitude recorded at YD Mine in 2021-2022.

Figure 5.7 shows a 3D view of the mine showing the principal regional pillar. In the new model, three lithologies replace the single rockmass material from the previous model. They are sediments, basalt/syenite, and diabase. The latter simulates the dykes. The total number of grid points from the model is 6,590,162. Figure 5.8 shows the updated model with the 3 lithologies. For the generation of the numerical model geometries, an octree mesh was created to replace the previous

model geometry. The model zones are densified according to the imported DXF geometries. The final model has a minimum mesh size of 0.6 m and a maximum of 12 m as the mesh approaches the external boundaries. Table 5.7 reports the rockmass properties used in the numerical model for linear elastic analysis.

Figure 5.7: 3D view of the YD Mine.

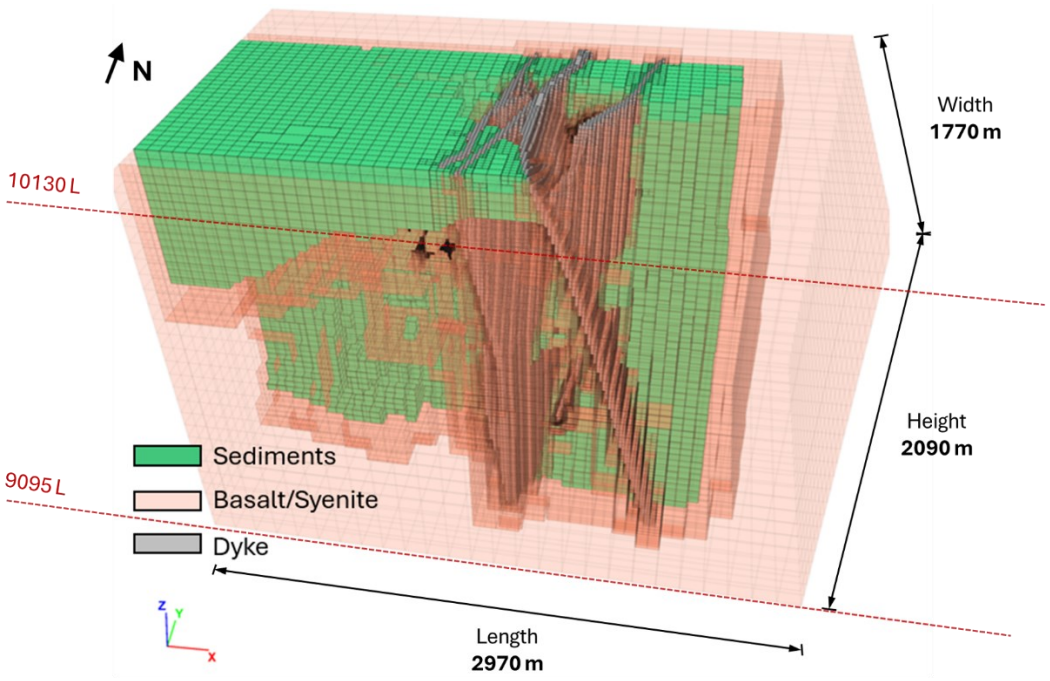

Figure 5.8: Updated numerical model with the new information from the lithologies.

Table 5.7: Mechanical properties of the geomaterials used in the numerical model.

Material	Rock Mass Modulus of Elasticity (GPa)	UCS (in MPa)	ν
Basalt/Syenite	45.9	146.3	0.3
Sediments	41.6	96.9	0.2
Diabase	35.1	118.5	0.2
Backfill	0.2	-	0.25

For the far field stress regime, it is based on research at YD Mine using the core deformation technique conducted on level 9130 by Li et al. (2024). The far field stress distribution is given by equations 5.3, 5.4 and 5.5 below (Khalil et al., 2024).

$$\sigma_1 = -0.065X + 677.84 \tag{5.3}$$

$$\sigma_2 = 0.028X + 6.39 \tag{5.4}$$

$$\sigma_3 = 0.028X - 47.72 \tag{5.5}$$

In the above, X is the depth in the units of the mine levels in meters, e.g. X = 9440 for a depth of 860 m below ground surface. It is noteworthy that according to Equations 5.3 and 5.5, the ratio between the major horizontal and vertical stresses is quite high, approaching 3. It is also important to note that, according to Li et al. (2024), the horizontal major principal stress direction is oriented at N45°E while the orebody strike runs in the East-West direction.

Regarding the mining sequence, due to the large number of historical stope sequencing, they were lumped into 11 modelling steps representing the initial (pre-mining) stress condition followed by 10 steps of stope extraction and backfilling. Historical stope production before the first occurrence of the seismic events was grouped in one step. Following that, 9 modelling steps were simulated to correspond to the occurrence of seismic events identified by Khalil et al. (2024). Modelling of backfilling sequence followed the actual schedule which was provided by the YD Mine. The backfill properties were also provided by the mine. Figure 5.9 shows the entire set of modeling steps representing the mining sequence leading to the seismic events of this study.

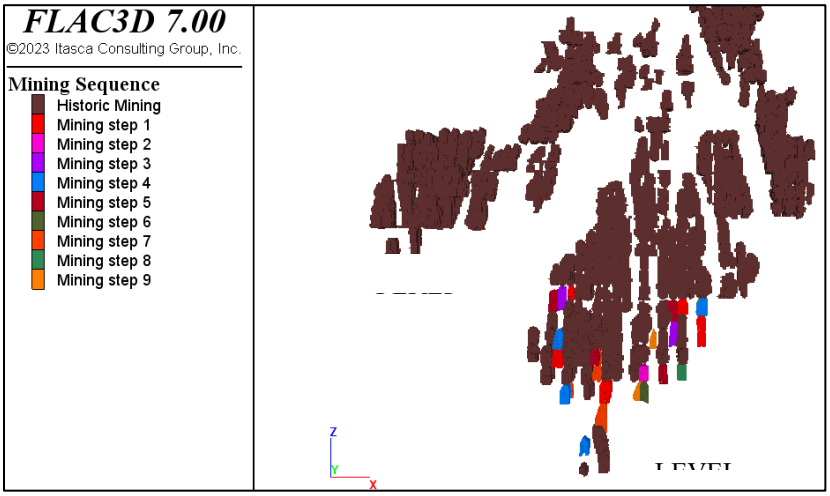

Figure 5.9: Modelling steps of the Young-Davidson Mine updated model.

5.6 Results

To assess burst potential from a linear elastic analysis, the Brittle Shear Ratio (BSR) proposed by Castro et al. (2012) is adopted. It is defined as the ratio of the deviatoric stress (or the difference between the major and minor principal stresses) to the UCS as shown in Equation 6 below.

$$Brittle\ Shear\ Ratio\ (BSR) = \frac{\sigma_1 - \sigma_3}{UCS} \tag{5.6}$$

Where σ_1 and σ_3 are the major and minor principal stresses, respectively. Castro et al. (2012) established thresholds for BSR to categorize strainburst potential as shown in Table 5.8.

Table 5.8: Ranges of BSR values and associated rock mass damage and potential strainburst (Castro et al., 2012).

BSR	Rock mass damage	Potential for strainburst
< 0.35	No to minor	No
0.35 to 0.45	Minor (surface spalling is a potential case)	No
0.45 to 0.6	Moderate (breakout formation expected)	Minor
0.6 to 0.7	Moderate to Major	Moderate
> 0.7	Major	Major

In the current study, nine seismic events reported by Khalil et al. (2024) are considered in this study. The magnitude, location, and date of each event are listed in Table 5.9. Since sesimic source calculations are often not precise due to the inherent heterogenity of the rockmass, it was decided, for the purpose of BSR maximum value estimation, that a radius of 20 m around the source location be searched for the highest BSR value. Numerical results in terms of maximum BSR values are presented in Table 5.9. Figures 5.10, 5.11 and 5.12 display the BSR contour lines with the seismic source locations superposed on the graphical model output. It is found that the numerical model predictions of BSR > 0.7 correlate well with 5 seismic events namely #2, 4, 5, 7, and 8. Figures 5.10, 5.11, and 5.12 demonstrate the overlap of high BSR zones with the seismic source location for events 4, 5, and 6. Table 5.9 also reports the location of each seismic source. It is noted that 6 of the 9 events took place in the ore, i.e. in ore blocks to be mined as secondary stopes. This may be explained by the high stress concentration around the mined primary stope as shown in the plan view of stope, which is due to the high primary horizontal in-situ stress and its oblique orientation to the orebody strike.

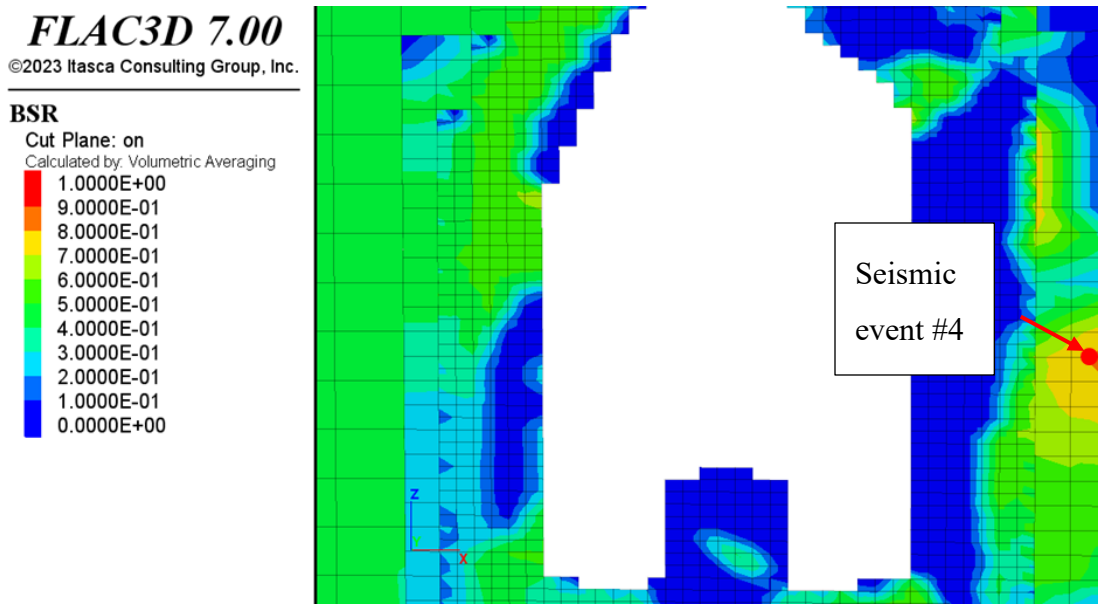

Figure 5.10: Assessment of BSR after the 4th modelling step – level 9375.

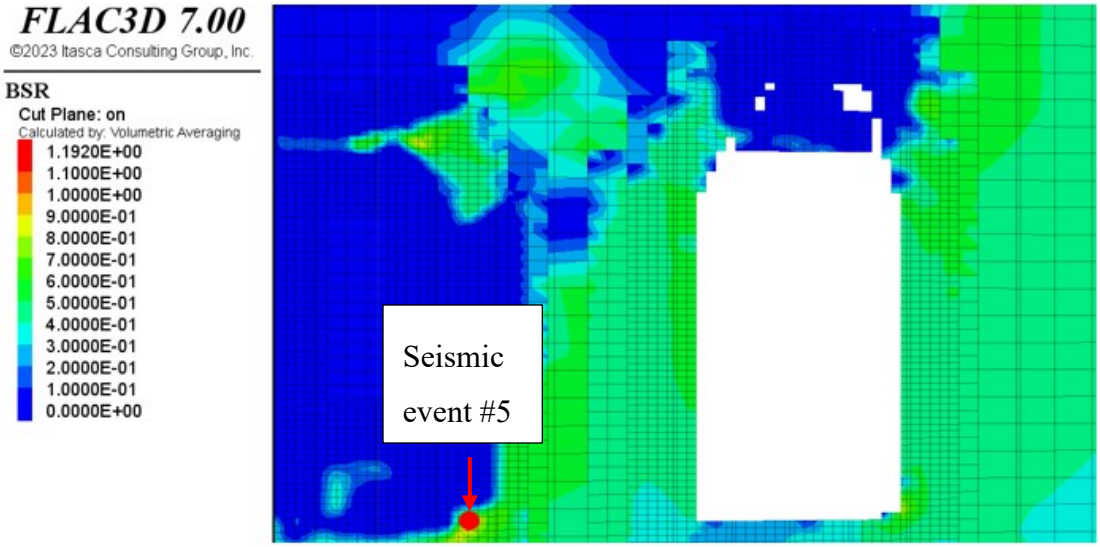

Figure 5.11: Assessment of BSR at the 5th modelling step – Level 9410.

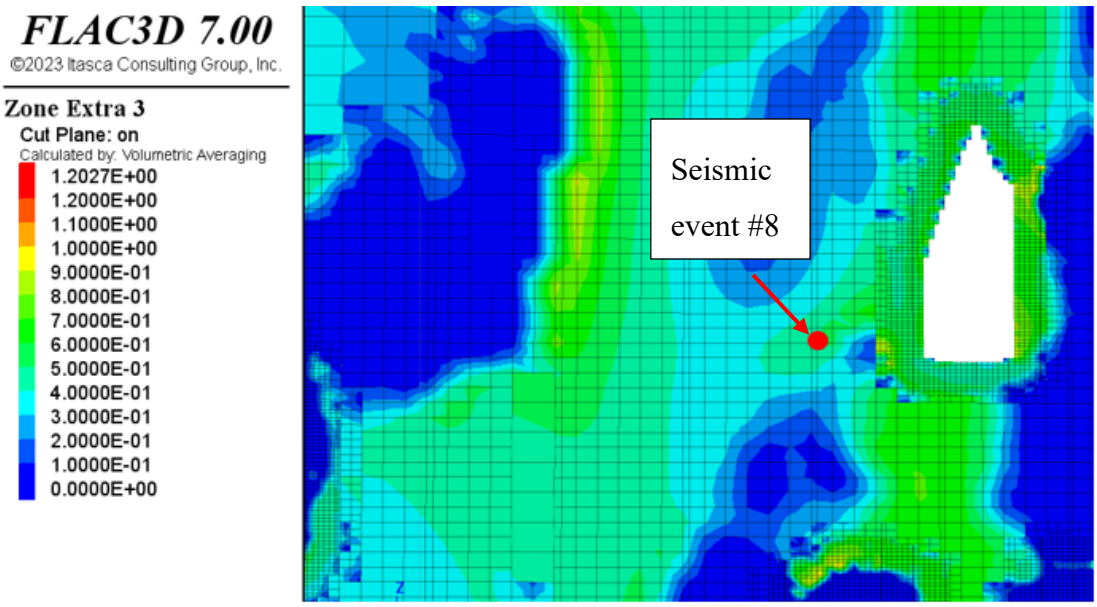

Figure 5.12: Assessment of BSR at the 8th modelling step – Level 9410.

Table 5.9: Results of BSR values around seismic source locations.

Event number	Event date	Magnitude Moment (Mn)	Depth–easting	Location of the event	Lithology	Modelling step	BSR value
1	2/6/2022	2.02	9413-3250	Footwall	Sediments	1	0.58
2	5/6/2021	2.36	9434-3252	Footwall	Sheared sediments	2	0.75 > 0.7
3	5/17/2021	2.3	9396-3234	Ore	Syenite	3	0.46
4	6/30/2021	2.27	9381-3193	Ore	Syenite	4	1.02 > 0.7
5	7/18/2021	2.28	9407-3247	Ore	Syenite	5	1.21 > 0.7
6	8/26/2021	2.03	9357-3250	Hanging wall	sediments	6	0.64
7	9/4/2021	2.07	9249-3246	Ore	Syenite	7	0.81 > 0.7
8	10/16/2021	2.39	9393-3294	Ore	Syenite	8	1.23 > 0.7
9	2/10/2022	2.02	9288-3218	Ore	Syenite	9	0.61

Based on these results, it can be seen that the stress state is the primary driver for triggering seismicity in the orebody, hanging wall, and footwall at YD Mine. In the absence of geological structures, and given that the lithologies of the YD Mine are not burst-prone, it can be concluded that mining goemetry is likely to be the main cause. However, according to YD Mine, most large events have a strong shear component, which suggests the presence of geological features in the ore pillars that are not accounted for in this study.

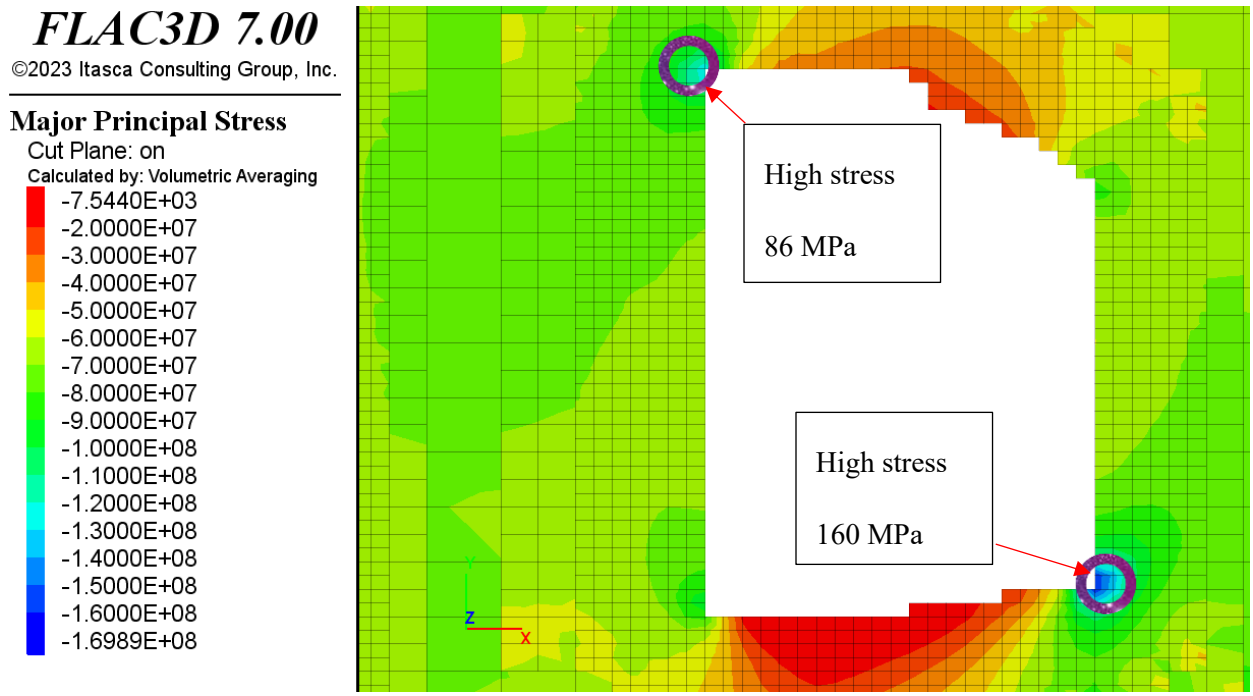

Figure 5.13: Plan view at mid-height of stope 3490-9410, 8th modelling step. Note: negative values mean compression.

5.7 Conclusions

In this study, it is shown that the high horizontal-to-vertical stress ratio can be a significant cause for mining-induced seismicity. This is an addition to the geological anomalies in the ore pillars that were not explicitly modelled in this study. First, rock burstability is examined through a comprehensive rock testing program of the different YD Mine lithologies. The program encompassed BTS, UCS, and LUN tests. It is found rock burstability potential is low to moderate at best. A 3D mine-wide numerical model was then built, and the updated mechanical rock properties were used. The stress analysis revealed that high stress concentration occurs in the ore pillars leading to high BSR values. Good correlation between predicted maximum BSR (> 0.7)

and seismic source location was obtained for 5 out of 9 events. Seismic source locations were found to be in the ore and developments. Seismic events were attributed primarily due to two factors. First, the major principal horizontal in-situ stress tensor has an oblique orientation to the orebody strike with an exceptionally high horizonal to vertical stress in-situ stress ratio. Secondly, according to YD mine records, strong seismic events contain a strong shear component, which suggests the presence of geological anomalies in the orebody and footwall. These findings support the hypothesis that strong mining-induced seismicity can still occur in underground mines regardless of rock properties.

Acknowledgement

This research was financially supported by Alamos Gold Inc. through a MITACS Project No. IT30669 ACC. The authors are grateful for their support.

References

American Society for Testing and Materials International. 2016. ASTM – D3967-16 Standard test method for splitting tensile strength of intact rock core specimens. Committee D18 on Soil and Rock, Subcommittee D18.12 on Rock Mechanics.

Butcher, R., Moran, T., McLeay, G. 2005. Long shaft – A deep level mining success story. Ninth Underground Operators Conference, Perth, Western Australia, 187-191.

Blake, W., Hedley, D. 2009. Rockbursts: Case Studies from North American Hard-Rock mines. Society for Mining, Metallurgy and Exploration, Colorado, USA.

Cai, M. 2016. Prediction and prevention of rockburst in metal mines – A case study of Sanshandao gold mine. Journal of Rock Mechanics and Geotechnical Engineering, vol. 8, pp. 204 – 211. http://dx.doi.org/10.1016/j.jrmge.2015.11.002.

Castro, L., Bewick, R., Carter, T. 2012. An overview of numerical modelling applied to deep mining. Innovative Numerical Modelling in Geomechanics, CRC Press, London, UK, 393 - 414.

Dunlop, R., Gaete, B. 2001. An estimation of the induced seismicity related to a caving method. Rockbursts and Seismicity in Mines. Dynamic rock mass response to mining, South African Institute Min. Metal, Johannesburg. pp. 281-285.

Gibowicz, S. 1990. Seismicity induced by mining. Advances in Geophysics, vol. 32, pp. 1-74. https://doi.org/10.1016/S0065-2687(08)60426-4.

Guha, S. 2000. Induced Earthquakes. Springer Dordrecht. Ch. 5: Mining Induced Seismicity, pp. 159 – 215. https://doi.org/10.1007/978-94-015-9452-3.

Heal, D., Potvin, Y. 2006. Evaluating Rockburst Damage Potential in Underground Mining. Conference: 41st US Symposium on Rock Mechanics (URSMS). Golden, Colorado.

Hedley, D. 1992. Rockburst handbook for Ontario hard rock mines. CANMET Special report SP92-1. Ottawa. Energy, Mines and Resources, Canada.

Holub, K. 1997. Predisposition to induced seismicity in some Czech coal mines. Pure and Applied Geophysics. Vol. 150, pp. 435-450. https://doi.org/10.1007/s000240050086.

Itasca Consulting Group, Inc. 2019, FLAC3D — Fast Lagrangian Analysis of Continua in Three-Dimensions, Version 7.0, Minneapolis: Itasca.

Khalil, H., Chen, T., Blake, T., Thomas, A., Mitri, H. 2024. Analysis of induced seismicity at Young-Davidson Mine. Deep Mining 2024. Australian Centre for Geomechanics, Perth.

Kidybinski, A. 1981. Bursting liability indices of coal. International Journal of Rock Mechanics and Mining Sciences & Geomechanics Abstracts. Vol. 18, 4, 295-304. https://doi.org/10.1016/0148-9062(81)91194-3" \t "_blank" \o "Persistent link using digital object identifier.

Li, S., Zheng, W., Trifu, C., Leslie, I. 2005. Implementation of a multi-channel microseismic monitoring system at Fankou lead-zinc mine, China. Controlling seismic risk. Rockburst and seismicity in Mines, Australian Centre for Geomechanics, pp. 613-616. https://doi.org/10.36487/ACG_repo/574_69.

Li, Y., Chen, T., Blake, T., Mitri, H. 2024. Validation of diametrical core deformation technique for mining-induced stress estimation: a case study. Rock Mechanics and Rock Engineering, pp. 1-10.

Malki, J., Vennes, I., Rowe, C., Mitri, H. 2024. Evaluation of Rock Burstability with Mechanical Property testing and Microscopic Image Analysis. Rock Mechanics and Rock Engineering.

Mendecki, A. 1997. Seismic Monitoring in mines. Published by Chapman and Hall. https://doi.org/10.1007/978-94-009-1539-8.

Morrison, D., Galbraith, J. 1990. A case history of Inco's Copper Cliff North Mine. Rock Mechanics contributions and challenges. Rotterdam: A.A. Balkema, 51-58.

Neyman, B., Szecowka, Z., Zuberek, W. 1972. Effective methods for fighting rockbursts in polish collieries. In Proceedings of the 5th International Strata Control Conference, 23, 1-9.

Peng, Z., Wang, Y., Li, T. 1996. Griffith theory and rock burst criterion. Chinese Journal of Rock Mechanics and Engineering, vol. 15, 491-495.

Wang, J., Park, H. 2001. Comprehensive prediction of rockburst based on analysis of strain energy in rocks. Tunnelling and Underground Space Technology, 16, 49-57. https://doi.org/10.1016/S0886-7798(01)00030-X.

Zhang, J., Fu, B., Li, Z., Song, S., Shang, Y. 2012. Criterion and Classification for Strain Mode Rockbursts based on Five-factor comprehensive method. The Chinese Society for Rock Mechanics and Engineering. Beijing, China.

Chapter 6 - Conclusion

6.1 Summary of conclusions

This research examined a case study of the Macassa Mine of Agnico Eagle Ltd. in northern Ontario, Canada for the safe recovery of an ore sill pillar situated 1,700 m below surface. The sill pillar is planned for extraction with a longhole stoping method. Past mining activities employed cut-and-fill methods. To assess the stress condition in the pillar, a 3D mine wide numerical model was created with FLAC3D finite difference code. Numerical modelling results demonstrate a stable ore pillar during pre-mining and post blast within the sill pillar. The brittle shear ratio (BSR) and the burst potential index (BPI) were adopted to evaluate rockburst potential in the sill pillar and access developments. The results indicate the core of the pillar during overcut and undercut developments is below the BSR = 0.6 and BPI = 0.2 thresholds for generating critical particle ejection velocities. Higher BSR and BPI values compared to the pillar core were predicted within 2 m of the excavation surfaces but still showed BSR < 0.6 and BPI < 0.2 thresholds. The results agree with field observations and the seismic response from the sill developments and longhole drilling activities. Therefore, the use of BSR and BPI indices is validated for seismic hazard assessment.

The second part of this thesis is a case study from the Young Davidson (YD) Mine of Alamos Gold Inc. where strong seismic activities have been observed to occur at relatively shallows depths of less than 1 km. An extensive literature review has identified the principal reasons behind the occurrence of strong seismic activities leading to rockburst events in underground mines. They are 1) the mechanical rock properties of lithologies, 2) the presence of geological structures such as faults and dykes, and 3) mining parameters like stope size, orientation, and sequencing. The case study research involved a comprehensive rock testing program aimed at determining rock burstability of different lithologies. This was followed by a numerical modelling study of mining and filling sequence leading to stress distribution in the areas around seismic source locations. It is found that model predictions of rockburst potential using the BSR is aligned with seismic source locations of high moment magnitude.

The following conclusions can be drawn from this study.

- The study at Macassa Mine has demonstrated the effectiveness of BSR and BPI as useful indices to assess burst potential.
- Modelling the history of mining and filling in the Macassa Mine numerical model proved essential as it ultimately reproduced the field results observed.
- Derived kinetic energy and dynamic support capacity calculations at Macassa Mine indicate that the selected rock support system is ideal.
- To assess rock burstability at the YD Mine, a series of tests was conducted on six lithologies to determine uniaxial compressive strength (18 tests), 64 Brazilian Tensile Strength (64 tests) and strain energy storage index (23 tests).
- Based on the test results, it was concluded that the YD Mine lithologies have low to moderate potential for violent and brittle failure.
- Modelling the history of mining and filling in the YD Mine numerical model proved essential as it led to high BSR values in the vicinity of recorded seismic events.
- The stress analysis showed high stress concentrations occur in the ore and developments, away from the diabase dykes – the main geological feature at YD Mine.
- These results suggest the relevance of mining geometry such as stope size, orientation and sequence, as an independent cause for mining-induced seismicity.

6.2. Suggestions for future research

Based on the findings from the research of the present thesis, further research is suggested on the following topics.

- The combination of different parameters for seismicity and bursting events such as geological features and mining geometry.
- Further testing on the lithologies in the mines. Correctly assessing the mechanical properties of the materials is important to determine burstability. Numerical models need to represent lithologies as well as their properties.
- Current tools and indices do not show the behavior of events near the drift walls in the case of bursting events. In these cases, there is little confinement happening at the rock mass where the event occurs. This statement means that uniaxial testing results might not be enough to represent the stress state of the theoretical event.

References

1. Adushkin, V., Lovchikov, A., Goev, A. 2022. The Occurrence of a Catastrophic Rockburst at the Umbozero Mine in the Lovozero Massif, Central Part of the Kola Peninsula. Seismology. Vol. 504, 305-309.
2. Bates, R., Jackson, J. 1984. Dictionary of geological terms. The American Geological Institute. 3rd ed.
3. Bewick, R., Valley, B., Runnalls, S., Whitney, J., Krynicki, Y. 2009. Global approach to managing deep mining hazards. Proceedings of the 3rd CANUS Rock Mechanics Symposium, Toronto.
4. Blake, W. 1972. Rock-burst mechanics. Quarterly of the Colorado School of Mines, vol. 67, no. 1, pp. 1–64.
5. Blake, W., Hedley, D. 2009. Rockbursts: Case Studies from North American Hard-Rock mines. Society for Mining, Metallurgy and Exploration, Colorado, USA.
6. Butcher, R., Moran, T., McLeay, G. 2005. Long shaft – A deep level mining success story. Ninth Underground Operators Conference, Perth, Western Australia, 187-191.
7. Cai, M. 2016. Prediction and prevention of rockburst in metal mines – A case study of Sanshandao mine. Journal of Rock Mechanics and Geotechnical Engineering. Vol. 8, 2, 204-211.
8. Cai, M., Kaiser, P. 2018. Rockburst Phenomenon and Support Characteristics. Rockburst Support – Reference Book. Vol. 1.
9. Canadian Rockburst Research Program. 1996. A comprehensive summary of five years of collaborative research on rock bursting in hard rock mines. CAMIRO Mining Division.
10. Castro, L., Bewick, R., Carter, T. 2012. An overview of numerical modelling applied to deep mining. Innovative Numerical Modelling in Geomechanics, CRC Press, London, UK, 393 - 414.
11. Cook, N. 1965. A note on rockbursts considered as a problem of stability. Journal of the South African Institute of Mining and Metallurgy. Vol. 65, 8.
12. Durrheim, R., Roberts, M., Haile, A., Hagan, T., Jager, A., Handley, M., Spottiswoode, S., Ortlepp, W. 1998. Factors influencing the severity of rockburst damage in South African gold mines. Journal of South African Inst. Min. Metal. 53-58.

13. Durrheim, R. 2010. Mitigating the risk of rockbursts in the deep hard rock mines of South Africa: 100 years of research. Extracting the science: A century of mining research, 156-171.

14. Gill, D., Aubertin, M., Simon, R. 1993. A practical engineering approach to the evaluation of rockburst potential. In Proceedings of the 3rd International Symposium on Rockbursts and Seismicity in Mines, Proceedings of the 3rd International Symposium on Rockbursts and Seismicity in Mines, Rotterdam, Netherlands, pp. 63–68.
15. Gong, F., Wang, Y., Wang, Z., Pan, J., Luo, S. 2021. A new criterion of coal burst proneness based on the residual elastic energy index. International Journal of Mining Science and Technology. Vol. 31, pp. 553-563.
16. Google Maps. (2025). Google Maps.
17. Gu, R. 2013. Distinct element model analyses of unstable failures in underground coal mines. Mine Theses & Dissertations. Colorado School of Mines.
18. Guntumadugu, D. 2013. Methodology for the design of dynamic rock supports in burst prone ground. PhD thesis, McGill University, Montreal, Canada.
19. Hasegawa, H., Wetmiller, R., Gendzwill, D. 1989. Induced Seismicity in Mines in Canada – An overview. Pure Appl. Geophys. 129, 423-453. Birkhäuser Verlag, Basel.

20. He, F. 2005, Study on geological hazards in tunnelling of deep-buried long tunnels at Ginling-Dabashan orogen of the three gorges reservoir water diversion project, PhD thesis, China Academy of Geological Sciences, Beijing.
21. He, M., Miao, J., Li, D., Wang, C. 2007. Experimental study of rockburst processes of granite specimen at great depth. Chinese Journal of Rock Mechanics and Engineering, vol. 26, no. 5, pp. 865–876.
22. He, M., Ren, F., Liu, D. 2018. Rockburst mechanism research and its control. International Journal of Mining Science and Technology, vol. 28, 5, 829-837.
23. He, M., Xia, H., Jia, X., Gong, W., Zhao, F., Liang, K. 2012. Studies on classification, criteria and control of rockbursts. Journal of Rock Mechanics and Geotechnical Engineering, vol. 4, no. 2, pp. 97–114.
24. Heal, D., Potvin, Y. 2006. Evaluating Rockburst Damage Potential in Underground Mining. Conference: 41st US Symposium on Rock Mechanics (URSMS). Golden, Colorado.

25. Heal, D. 2010. Observations and analysis of incidents of rockburst damage in underground mines. PhD Thesis. The University of Western Australia, School of Civil and Resource Engineering. Australia.
26. Hedley, D. 1992. Rockburst handbook for Ontario hardrock mines. CANMET Special report SP92-1. Ottawa. Energy, Mines and Resources, Canada.
27. Hoek, E., Carranza-Torres, C., Corkum, B. 2002. Hoek-Brown failure criterion – 2002. In R Hammaah, W Bawden, J Curran & M Telesnicki (eds), Proceedings of the Fifth North American Rock Mechanics Symposium (NARMS-TAC), University of Toronto Press, Toronto, pp. 267-273.
28. Itasca Consulting Group, Inc. 2019, FLAC3D — Fast Lagrangian Analysis of Continua in Three-Dimensions, Version 7.0, Minneapolis: Itasca.
29. Jaeger, J., Cook, N. 1979. Fundamentals of Rock Mechanics, 3rd ed. Chapman & Hall, London.
30. Kaiser, P., Tannant, D., McCreath, D. 1996. Canadian Rockburst Support Handbook. Geomechanics Research Centre, Laurentian University, Sudbury, Ontario.
31. Keneti, A., Sainsbury, B. 2018. Review of published rockburst events and their contributing factors. Engineering Geology, 246, 361-373.
32. Kidybinski, A. 1981. Bursting liability indices of coal. International Journal of Rock Mechanics and Mining Sciences & Geomechanics Abstracts. Vol. 18, 4, 295-304.
33. Khalil, H. 2023. Effect of mining and geology on induced seismicity – A case study. Master's Thesis. McGill University, Montreal, Quebec, Canada.
34. Khalil, H., Chen, T., Blake, T., Thomas, A., Mitri, H. 2024. Analysis of induced seismicity at Young-Davidson mine. Deep Mining 2024. Australian Centre for Geomechanics, Perth.
35. Li, S., Feng, X., Wang, Y., Yang, N. 2001. Evaluation of rockburst proneness in a deep hard rock mine. J. Northeast Univ. (National Sciences), 22, 1, 60-63.
36. Li, C., Mikula, P., Simser, B., Hebblewhite, B., Joughin, W., Feng, X., Xu, N. 2019. Discussions on rockburst and dynamic ground support in deep mines. Journal of Rock Mechanics and Geotechnical Engineering, 11, 1110-1118.
37. Li, Y., Chen, T., Blake, T., Mitri, H. 2024. Validation of diametrical core deformation technique for mining-induced stress estimation: a case study. Rock Mechanics and Rock Engineering, pp. 1-10.

38. Lu, C., Liu, Y., Zhang, N., Zhao, T., Wang, H. 2018. In-situ and experimental investigation of rockburst precursor and prevention induced by fault slip. International Journal of Rock Mechanics and Mining Sciences, 108, 86-95.
39. Malki, J., Vennes, I., Rowe, C., Mitri, H. 2024. Evaluation of Rock Burstability with Mechanical Property testing and Microscopic Image Analysis. Rock Mechanics and Rock Engineering.
40. Manouchehrian, A., Cai, M. 2018. Numerical modeling of rockburst near fault zones in deep tunnels. Tunnelling and Underground Space Technology, vol. 80, 164-180.
41. Martin, D., Chandler, N. 1996. The potential for Vault-Induced Seismicity in nuclear Fuel Waste Disposal: Experience from Canadian Mines. AECL Research, 11599.
42. McGarr, A. 1997. A mechanism for high wall-rock velocities in Rockbursts. Pure and Applied Geophysics, vol. 150, pp. 381-391.
43. Mikula, P. 2012. Progress with empirical performance charting for confident selection of ground support in seismic conditions. Sixth International Seminar on Deep and High Stress Mining.
44. Mikula, P., Lee, M. 2002. Forecasting and controlling pillar instability at Mount Charlotte Mine. The 1st International Seminar on deep and High stress mining, 20, Australian Centre for Geomechanics, Perth.
45. Mitri, H., Tang, B., Simon, R. 1999. FE modelling of mining-induced energy release and storage rates. The Journal of the South African Institute of Mining and Metallurgy, 99, 2, 103 - 110.
46. Mitri, H. 2007. Assessment of horizontal pillar burst in deep hard rock mines. International Journal of Risk Assessment and Management, vol. 7, 5, 695-707.
47. Mitri, H. 2018. Destress Blasting – From Theory to Practice. Proceedings of the 4th World Congress on Mechanical, Chemical, and Material Engineering.
48. Morrison, D., Galbraith, J. 1990. A case history of Inco's Copper Cliff North Mine. Rock Mechanics contributions and challenges. Rotterdam: A.A. Balkema, 51-58.
49. Neyman, B., Szecowka, Z., Zuberek, W. 1972. Effective methods for fighting rockbursts in polish collieries. In Proceedings of the 5th International Strata Control Conference, 23, 1-9.

50. Ortlepp, W. 1992. Invited lecture: The design of support for the containment of rockburst damage in tunnels – An engineering approach. Proceedings of Rock Support and Underground Construction, Rotterdam, A.A. Balkema, pp. 593-609.
51. Ortlepp, W. 1994. Rockburst Mechanism in Tunnels and Shafts. Tunnelling and Underground Space Technology, Vol. 9, No. 1, pp-59-65.
52. Ortlepp, W. 1997. Rock fracture and rockbursts, an illustrative study. Johannesburg, SAIMM Monogr. Ser. M9, 98.
53. Ortlepp, W. 2005. RaSiM Comes of age – A review of the contribution to the understanding and control of Mine rockbursts. Proceedings of the Sixth International Symposium on Rockburst and Seismicity in Mines proceedings, Australian Centre for Geomechanics, Perth, 3-20.
54. Peng, Z., Wang, Y., Li, T. 1996. Griffith theory and rock burst criterion. Chinese Journal of Rock Mechanics and Engineering, vol. 15, 491-495.
55. Rong, H., Li, N., Zhang, H., Sun, D., Huo, B. 2022. Insights into fundamental problems of rockburst under the modern structure stress field. Scientific Reports, 12, 20299.
56. Solak, T. 2009. Ground behavior evaluation for tunnels in blocky rock masses. Tunnelling and Underground Space Technology, vol. 24, no. 3, pp. 323–330.
57. Varden, R., Lachenicht, R., Player, J., Thompson, A., Villaescusa, E. 2008. Development and implementation of the Garford dynamic bolt at the Kanowna Belle Mine. 10th underground operators' conference, Launceston, Australia.
58. Vennes, I., Mitri, H., Chinnasane, D., Yao, M. 2020. Large-scale destress blasting for seismicity control in hard rock mines: A case study. International Journal of Mining Science and Technology, vol. 30, 2, 141-149.
59. Venter, J., Purvis, C., Hamman, J. 2016. Hoek-Brown mi estimation – a comparison of multistage triaxial with single stage triaxial testing. APSSIM 2016: Proceedings of the First Asia Pacific Slope Stability in Mining Conference. Australian Centre for Geomechanics, Perth.
60. Wang, J., Park, H. 2001. Comprehensive prediction of rockburst based on analysis of strain energy in rocks. Tunnelling and Underground Space Technology, 16, 49-57.

61. Wu, M., Ye, Y., Wang, Q., Hu, N. 2022. Development of Rockburst Research: A comprehensive Review. Applied Sciences, 12, 3.

62. Zhang, J., Fu, B., Li, Z., Song, S., Shang, Y. 2011. Criterion and Classification for Strain Mode Rockbursts based on Five-factor comprehensive method. The Chinese Society for Rock Mechanics and Engineering. Beijing, China.

63. Zhou, J., Li, X., Mitri, H. 2018. Evaluation Method of rockburst: State-of-the-art Literature Review. Tunnelling and Underground Space Technology, 81, 632-659.

64. Zhou, H., Meng, F., Zhang, C., Hu, D., Yang, F., Lu, J. 2015. Analysis of rockburst mechanisms induced by structural planes in deep tunnels. Bulletin Eng. Geol. Environ., 74, 1435-1451.